Materials Today Advances 28 (2025) 100654

Contents lists available at ScienceDirect

Materials Today Advances

journal homepage: www.journals.elsevier.com/materials-today-advances/

Oxidation-driven structural, chemical and electrical transformation in $ZrSe_2$

Kimberly Intonti [a,b,*,1], Hazel Neill [c,1], Sharieh Jamalzadeh Kheirabadi [c], Zabeada Aslam [d], Timothy Moorsom [d], Joslin Sunder Prasanna [e], Rafik Addou [e], Luca Persichetti [f], Anna Sgarlata [f], Luca Camilli [f], Stephen O'Sullivan [c], Vilas Patil [c], Davinder Singh [c], Brendan Sheehan [c], Paul K. Hurley [c,g], Lida Ansari [c], Antonio Di Bartolomeo [a,**], Farzan Gity [c,***]

[a] Department of Physics "E. R. Caianiello", University of Salerno, via Giovanni Paolo II, Fisciano, Salerno, 84084, Italy
[b] CNR-SPIN Salerno, via Giovanni Paolo II, Fisciano, 84084, Italy
[c] Tyndall National Institute, University College Cork, Lee Maltings, Dyke Parade, Cork, T12 R5CP, Ireland
[d] School of Chemical and Process Engineering, University of Leeds, Leeds, UK
[e] Department of Materials Science and Engineering, University of Texas at Dallas, USA
[f] Dipartimento di Fisica, University of Rome "Tor Vergata", via della Ricerca Scientifica 1, 00133, Rome, Italy
[g] School of Chemistry, University College Cork, Cork, Ireland

A B S T R A C T

The intrinsic air sensitivity of two-dimensional (2D) transition metal dichalcogenides (TMDs) poses a major challenge for their deployment in nanoelectronics devices. In this work, we present a comprehensive study of the oxidation-driven degradation of $ZrSe_2$, revealing the time-dependent evolution of surface morphology, chemical composition, and device performance. Using a suite of experimental techniques including AFM, SEM, STM, EDX, XPS, and Raman spectroscopy, complemented by density functional theory (DFT) simulations, we track the spontaneous formation of Se-rich protrusions and nanowires resulting from oxidation. Our findings demonstrate that oxidation initiates both at defect sites and edges, leading to the formation of a native Zr oxide that promotes selenium segregation. EDX confirms Se-rich blisters and nanowires, while Raman spectroscopy reveals the loss of $ZrSe_2$ vibrational modes and the emergence of Se peaks over time. DFT results further explain this behaviour by showing that oxygen adsorption weakens Zr-Se bonds and facilitates Se clustering. Encapsulation with a thin e-beam evaporated ZrO_2 layer limits degradation and offers a path toward improved field-effect transistor performance under optimized conditions. This work provides new insights into the degradation pathways of $ZrSe_2$ and underscores the critical importance of interface engineering and environmental control for reliable 2D semiconductor devices.

1. Introduction

Two-dimensional (2D) semiconductors have attracted great attention for electronic devices, especially as alternatives to silicon, due to their potential to overcome short channel effects and provide new functionalities: Especially they enable ultrathin transistor channels with strong electrostatic control. Despite 2D materials such as MoS_2 [1], WS_2 [2] or BP [3] being successfully used in field effect transistors (FETs) with high on-off ratio and high performance, creating a smooth, defect-free interface between the 2D materials and gate dielectric is still a critical challenge. Defective interfaces between the 2D semiconductor and the gate oxide can limit device switching properties and reduce ON-state current. Therefore, the preparation of clean interfaces with the dielectric is considered one of the key bottlenecks to overcome before 2D semiconductors can be fully applied in electronic devices [4].

Among IV-B group transition metal dichalcogenides (TMDs), 2D materials like Zr and Hf selenides and sulphides have gained increasing interest as potential silicon substitutes because, in addition to their large work function and high mobility, they can benefit from their native oxides [5]. Their kinetic energy barrier for oxidation is, indeed, very low. Even a short exposure to ambient air causes these materials to oxidize quickly, leading to the formation of the respective transition metal oxides (TMOs) on their surface [6]. Having a high-k dielectric as a native oxide makes these materials even more advantageous than group VI TMDs, since they do not need to be combined with a dielectric of a different metal, thereby minimizing interfacial incompatibility with the

* Corresponding author.
** Corresponding author.
*** Corresponding author.
E-mail addresses: kintonti@unisa.it (K. Intonti), hazel.neill@tyndall.ie (H. Neill), adibartolomeo@unisa.it (A. Di Bartolomeo), farzan.gity@tyndall.ie (F. Gity).
[1] Joint first authors.

https://doi.org/10.1016/j.mtadv.2025.100654
Received 20 August 2025; Received in revised form 9 October 2025; Accepted 30 October 2025
Available online 6 November 2025

deposited oxides. Therefore, ZrX_2/ZrO_2 and HfX_2/HfO_2, where X is a chalcogen, are intriguing options for semiconductor/insulator heterostructures, such as Si/SiO_2, with the advantage that ZrX_2/HfX_2 are layered materials that can be reduced to ultrathin 2D layers [7].

However, to obtain a reliable and smooth 2D semiconductor/oxide interface, it is necessary to first comprehend in detail how the oxidation process manifests itself, on what time scale, how it impacts the material's morphology and whether it causes structural changes. Many 2D semiconductors, such as silicene [8], BP [9], and also some group VI-TMDs [10], exhibit a severe reaction to ambient air [11]. This reduces the device's performance because oxygen and water adsorption can significantly alter its physical, chemical and electronic properties [6,12], or even result in complete degradation. Understanding the fundamental aspects of the oxidation process would help in intentionally preventing 2D semiconductors from oxidation and in identifying appropriate methodologies to preserve them in specific conditions [13].

For IV-B group TMDs, as the radius grows from Ti to Hf, the mobility of MX_2 composites increases, but the air stability dramatically drops [11]. Theoretical calculations reveal that the oxidation preferably takes place at the flake edges with 50 % terminated in sulphur or is initiated by a sulphur vacancy [6]. This is confirmed by experimental works showing that the oxidation region grows around 80 nm into the flake of TiS_2 from the edges after 21 days in H_2O [14]. Other studies confirm that moisture, more than oxygen, is the main obstacle to long-term stability in these materials [15].

Hf-based composites also exhibit significant degradation when exposed to air. The surface of HfS_2 flakes displays small protrusions after oxidation while their thickness increases because of oxygen intercalation, according to optical images and AFM measurements [16]. Both humidity and oxygen molecules contribute to the occurrence of these features. In the case of $HfSe_2$, Hf is oxidizing into HfO_2, breaking the bonds with Se atoms that coalesce into blisters on the surface. The process is more dramatic and faster in $HfSe_2$ compared to HfS_2. Signs of degradation are visible on $HfSe_2$ flakes after 1 day, while 9 days are needed for HfS_2 [6].

The air stability of ZrX_2 is also notably poor. Raman measurements have been shown to be unreliable to identify monolayer/bilayer ZrS_2 and the Raman peak of thin flakes disappears after a couple of days [17,18]. As in the case of HfX_2, the oxidation effects on the selenide counterpart were observed to be even more significant. $ZrSe_2$ is particularly promising as it is a semiconductor with a bandgap of approximately 1 eV in its bulk form – similar to silicon – which increases to around 1.5 eV when reduced to a monolayer. A 1 eV bandgap is well-suited for low-voltage operation and helps to reduce direct tunnelling and leakage current [19]. Another notable feature of $ZrSe_2$ is its demonstrated negative differential resistance in nanoribbon form, which makes it a promising candidate for spintronic devices [20]. Its native oxide, ZrO_2, has a wide bandgap of 5.3 eV and belongs to the class of "high-k" dielectrics, which have increasingly replaced SiO_2 in modern electronics due to their higher dielectric constant. However, despite extensive efforts using various deposition and growth methods – including thermal and plasma oxidation – a reliable approach for obtaining a smooth, homogeneous TMO layer has yet to be established [21].

Controlling and tuning the formation of oxides constitutes a new area of study that uses oxidized 2D materials and their heterostructures in several fields, such as metal-semiconductor interfaces, van der Waals heterostructures, memristors and photonic devices [22], materials growth processes, engineering concepts, and investigation of new condensed matter phenomena [23].

In this work, we present a comprehensive, time-resolved study of the ambient degradation of $ZrSe_2$, with particular emphasis on the morphological and structural evolution induced by oxidation. Using complementary surface-sensitive techniques – including scanning electron microscopy (SEM), atomic force microscopy (AFM), scanning tunnelling microscopy (STM), and Raman spectroscopy – we capture both the early stages and long-term effects of air exposure, identifying the formation and transformation of Se-rich nanostructures over time. We further investigate the impact of electron-beam exposure on surface evolution, revealing that SEM scanning alters the natural oxidation progression. Chemical and structural analysis via STEM, EDX, and XPS confirms Se segregation and Zr oxidation, providing insights into blister formation and nanowire nucleation. To gain an atomistic understanding of these transformations, we perform density functional theory (DFT) simulations, which show how oxygen adsorption weakens Zr-Se bonds and promotes Se detachment and clustering – consistent with the emergence of Se-rich protrusions observed experimentally. To mitigate oxidation, we propose a ZrO_2 encapsulation strategy, enabling the fabrication of $ZrSe_2$-based field-effect transistors with promising mobility. Our findings, supported by density functional theory (DFT) simulations, uncover critical degradation pathways and propose practical strategies for stabilizing $ZrSe_2$ in device environments.

2. Methods

All the $ZrSe_2$ flakes were mechanically exfoliated from their bulk crystal using the scotch tape technique. The flakes on the scotch tape were then gently pressed on intrinsic silicon substrates or Si/SiO_2 (85 nm) substrates. AFM measurements were performed with Bruker AFM (Dimension Icon Model) in tapping mode using an FMV-A 7 nm tip to avoid any contact between the AFM tip and the surface. For each sample, a $20 \times 20\ \mu m^2$ scan was performed with 512 scan lines and a frequency of 0.4 Hz, trying to repeatedly scan the same location. The acquired data was analysed using Gwyddion Software. A Tescan Amber X FIB-SEM with Oxford Ultim Max Energy Dispersive X-ray Spectroscopy (EDX) was used for surface and elemental characterization. The energy of the beam was set to 5 keV and the BC was 1 nA to properly detect all the features of the surface. Raman spectra were acquired with a Horiba XploRA™ Plus confocal Raman microscope equipped with a 70 mW, 532 nm laser. All the Raman spectra, if not otherwise specified, were acquired with a power of 0.5 %, with an acquisition time of 10 s and an accumulation time of 10 s, using a 50x objective.

The cross-sectional lamellas were prepared using a Tescan Solaris Ga + DualBeam focused ion beam (FIB) system for high-resolution structural analysis. Prior to ion milling, protective layers were sequentially deposited over the region of interest to minimize beam-induced damage. The lamellas were then extracted and mounted onto a copper grid. Thinning to electron transparency was performed at an accelerating voltage of 30 kV, while final polishing was carried out at 5 kV using an in-situ ion beam to minimize surface damage and amorphization. Subsequent cross-sectional imaging was conducted directly on the Tescan Solaris system using dark-field scanning transmission electron microscopy (DF-STEM) at 30 kV, employing a 100 pA beam current in immersion mode, enabling measurement of structural features. All imaging and data acquisition were performed using the Essence™ software. Between the different measurements, all flakes under investigation have been stored in the cleanroom environment. STEM imaging and correlated EDX was performed on a Tescan Tensor rapid precession 4DSTEM microscope at an accelerating voltage of 100 kV, a probe current of 50 pA and a convergence angle of 9.78 mrad. The probe size during EDX measurement was 1.5 nm. Cross-sections were aligned to the Si substrate axis using a double tilt holder. EDX frame acquisition time was 56 µs. Between the different measurements, all flakes under investigation have been stored in the cleanroom environment.

X-ray Photoelectron Spectroscopy (XPS) was performed using a monochromatic Al Kα source ($E_k = 1486.7$ eV) and an Omicron EA125 hemispherical analyzer that was calibrated using three different metals Au (83.9 eV), Cu (932.6 eV), and Ag (368.2 eV). XPS spectra were acquired using a pass energy of 15 eV and an energy resolution of 0.05 eV $ZrSe_2$ crystals were then loaded into an ultra-high vacuum XPS chamber, with a base pressure of $\sim 2.0 \times 10^{-10}$ mbar. XPS analysis was conducted on a freshly exfoliated sample, an aged (oxidized) sample, and on a sample after 24 h of air exposure. The sample was exfoliated twice using

Scotch tape in a fume hood. It was then transferred to the load-lock chamber of the XPS instrument, where a final exfoliation was performed under N_2 atmosphere. The analysis of XPS data was conducted using the analytical software Analyzer [24].

Scanning tunnelling microscopy (STM) measurements were conducted on a bulk $ZrSe_2$ crystal exfoliated in the load-lock chamber of an ultrahigh-vacuum (UHV) system at a pressure of 5×10^{-7} mbar. The exfoliated sample was immediately transferred to the measurement chamber, maintained at a base pressure of 5×10^{-10} mbar. STM imaging was performed at room temperature in constant-current mode using an Omicron system equipped with an electrochemically etched tungsten tip. To assess the effects of air exposure, additional measurements were carried out on aged samples following exposure to ambient conditions for varying durations.

Density Functional Theory (DFT) calculations were performed using the Generalized Gradient Approximation (GGA) for the exchange-correlation potential, as implemented in the QuantumATK simulation package [25]. A medium-basis set Linear Combination of Atomic Orbitals (LCAO) approach was employed, utilizing GGA norm-conserving pseudopotentials from the PseudoDojo library [26]. For Brillouin zone integration, a k-point grid was generated using the Monkhorst-Pack scheme [27], achieving a density of approximately 10 k-points per $Å^{-1}$. An energy cutoff of 105 Hartree was applied to the discretized real-space grid. Van der Waals (vdW) interactions were included using the Grimme DFT-D3 dispersion correction method [28]. All atomic positions were fully relaxed during structural optimization until the residual forces on each atom were reduced below 1×10^{-2} eV/Å, ensuring well-converged geometries. A vacuum layer exceeding 2 nm was introduced in the in-plane direction to prevent interactions between periodic images of the nanoribbons, effectively simulating bulk-like behaviour.

Additional $ZrSe_2$ flakes were mechanically exfoliated onto Si/SiO_2 substrates (85 nm oxide thickness) within an inert atmosphere glovebox. The samples were subsequently transferred to an electron beam evaporator for encapsulation with a nominal 2 nm thick ZrO_2 film. Air exposure during this transfer process was strictly limited to approximately 40 s, solely for mounting the substrates into the evaporator. Following encapsulation, back-gated field-effect transistors (FETs) were fabricated by patterning and depositing Cr/Au (15/150 nm) contact electrodes via electron beam evaporation. All completed devices were stored in the glovebox between measurements to minimize ambient exposure.

3. Results and discussion

3.1. Time-dependent degradation process of $ZrSe_2$ under ambient conditions

This section summarizes the results of the continuous SEM/AFM investigation conducted for a month on mechanically exfoliated $ZrSe_2$ flakes, transferred on a Si substrate. In order to capture the initial stages of the oxidation process, the samples were loaded into the SEM immediately after exfoliation and were exposed to air only briefly - just long enough for the chamber to be pumped down (a few minutes). We selected large flakes with multiple terraces to maximize the exposed surface area and enable the examination of different types of edges, as shown in Fig. 1 and S1.

Fig. 1a shows a zoomed-out optical image of a representative $ZrSe_2$ flake - another example is provided in Section S.1 - highlighting its characteristic contrast on the Si substrate. The slight colour variations between the terraces correspond to differences in thickness. Immediately after exfoliation, $ZrSe_2$ exhibits early-stage degradation, as shown in the SEM image in Fig. 1b, even though the oxygen atomic percentage is below the EDX detection limit, according to the EDX spectrum in Fig. 1c. The Zr:Se stoichiometric ratio is approximately 0.61, indicating a non-stoichiometric composition and the presence of selenium vacancies, which likely act as adsorption sites for oxygen.

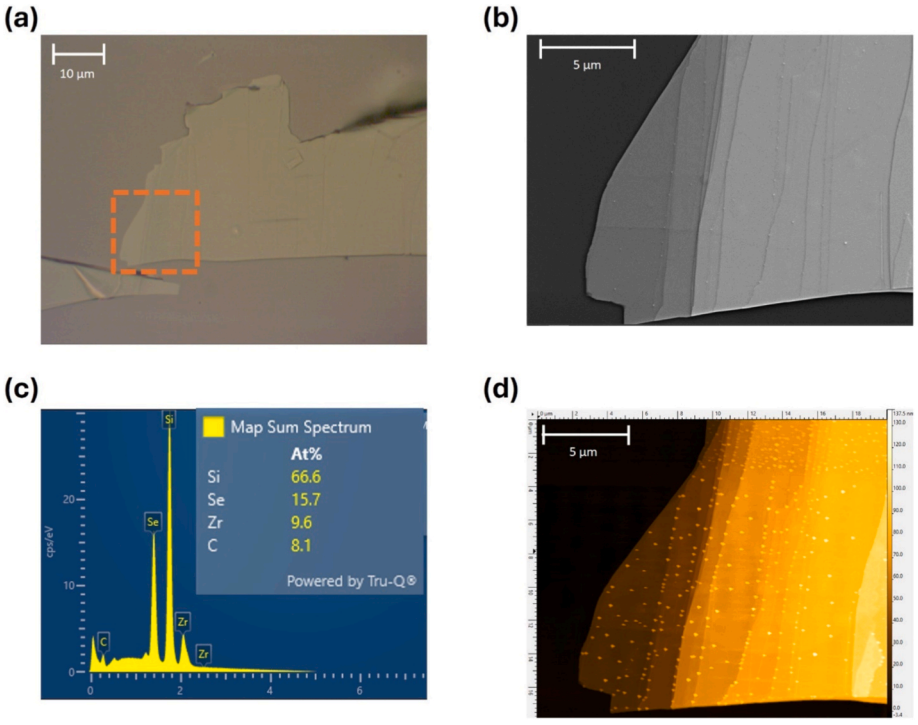

Fig. 1. Early signs of ambient oxidation. (a) Optical image of a freshly exfoliated $ZrSe_2$ flake. The dashed orange box indicates the region examined in subsequent analyses. (b) SEM image of the selected area taken within minutes of exfoliation, showing early-stage degradation. (c) EDX spectrum acquired from the same region. (d) AFM image acquired 3 h later, showing increased density of hemispherical protrusions (bright spots), mostly along step edges. These features correspond to raised structures, not pits, with heights up to ~35 nm. (For interpretation of the references to colour in this figure legend, the reader is referred to the Web version of this article.)

Numerous small hemispherical protrusions are located mainly along the step edges of the terraces, with some also scattered on the surface. Oxidation at the edges of 2D materials is a common phenomenon that has been previously reported [29,30]. The step-edges are optimal nucleation sites for the growth of these features because they contain broken bonds. The AFM measurement shown in Fig. 1d, carried out 3 h later, reveals a significantly higher density of these features, which appear prominently as white dots across both edge and surface regions. The AFM profile in Fig. S2 confirms that these protrusions are not holes, but raised features extending to a height of around 35 nm, which is thicker than the thinnest region of the flake.

The same AFM and SEM analyses were performed on different $ZrSe_2$ flakes 1, 5, 12 and 30 days after the exfoliation, shown in Fig. 2a, 2b, 2c, and 2d, respectively. For this study we selected multi-terraced flakes with similar thicknesses. Fig. 2a reveals that the degradation process is very fast, since a high density of protrusions has already formed after 24 h both at the edges and on the surface of the flake. Fig. 2b and 2c show a higher density of larger protrusions, compared with the freshly exfoliated flakes. However, the protrusions are not homogenously distributed over the surface. Indeed, some areas are clean, suggesting that this process is triggered by point defects on the surface rather than by the edges [31,32]. Even bigger protrusions are then clearly visible on the flake scanned after 30 days, revealing a persistent growth process of these features.

It was also seen using optical microscopy that the flakes in Fig. 2 underwent a dramatic colour change after the oxidation process, as shown in Fig. S3. The apparent colour of $ZrSe_2$ flakes, boosted by oxidation, has been investigated for both Si and Si/SiO_2 (85 nm) substrates in Section S.3. The colour variation - and the time scale over which it occurs - are strongly thickness dependent. Moreover, optical microscopy can also capture the development of the protrusions on the surface of the flakes.

The reason why measurements at specific time intervals after exfoliation were performed on different flakes rather than repeated on the same flake is that SEM dramatically modifies the surface of the flake when it is repeatedly scanned, interfering with the natural degradation process, as described in Section S.4. Therefore, for each flake in Fig. 2, SEM analysis was performed after acquiring AFM images.

To complement these results with atomic-scale information, we performed scanning tunnelling microscopy (STM) on freshly cleaved $ZrSe_2$ crystals. This technique allowed us to track surface changes during controlled air exposure with high spatial resolution. After an initial exfoliation under ultrahigh vacuum (UHV) conditions, a bulk $ZrSe_2$ crystal was subjected to successive air exposures of increasing time duration in the load-lock of the UHV system. Following each exposure, the sample was reintroduced into the analysis chamber under UHV conditions for STM measurements. The results are summarized in Fig. 3. The pristine sample exhibits an atomically flat surface with a root-mean-square (RMS) roughness of approximately 0.21 nm, measured over an 880 nm lateral area, as shown in Fig. 3a. A higher-magnification image over an $18 \times 18\ nm^2$ area clearly resolves the atomic lattice of $ZrSe_2$. The in-plane lattice parameter is 0.37 ± 0.02 nm, in good agreement with literature values [33,34].

After 4 min of air exposure, the surface roughness increases by a factor of ~3, while remaining sub-nanometric (Fig. 3b). The magnified view reveals the formation of numerous surface defects, primarily consisting of vacancy aggregates, often decorated with adsorbates and sub-nanometric clusters (see also Fig. S12). For longer air exposures, the atomic lattice is no longer visible, and the surface appears fully amorphous, with RMS roughness values reaching 4.88 nm and 7.39 nm after 17 and 47 min of total exposure, respectively (Fig. 3c and 3d). Interestingly, after 17 min, the surface corrugation becomes anisotropic, which is also evident in the corresponding Fast Fourier Transform (FFT) image as shown in the inset of Fig. S13(a). This anisotropy is lost after 47 min, with the surface appearing rougher and the FFT showing isotropy (Fig. S13(b)).

3.2. *Oxidation-induced Se segregation and blister formation*

While sections 1 and 2 concentrate on the initial phases of oxidation, immediately after exfoliation, this section investigates the oxidation process over extended exposure times. Fig. 4 shows a remarkable transformation in the morphology of the $ZrSe_2$ flake, after prolonged exposure to ambient air.

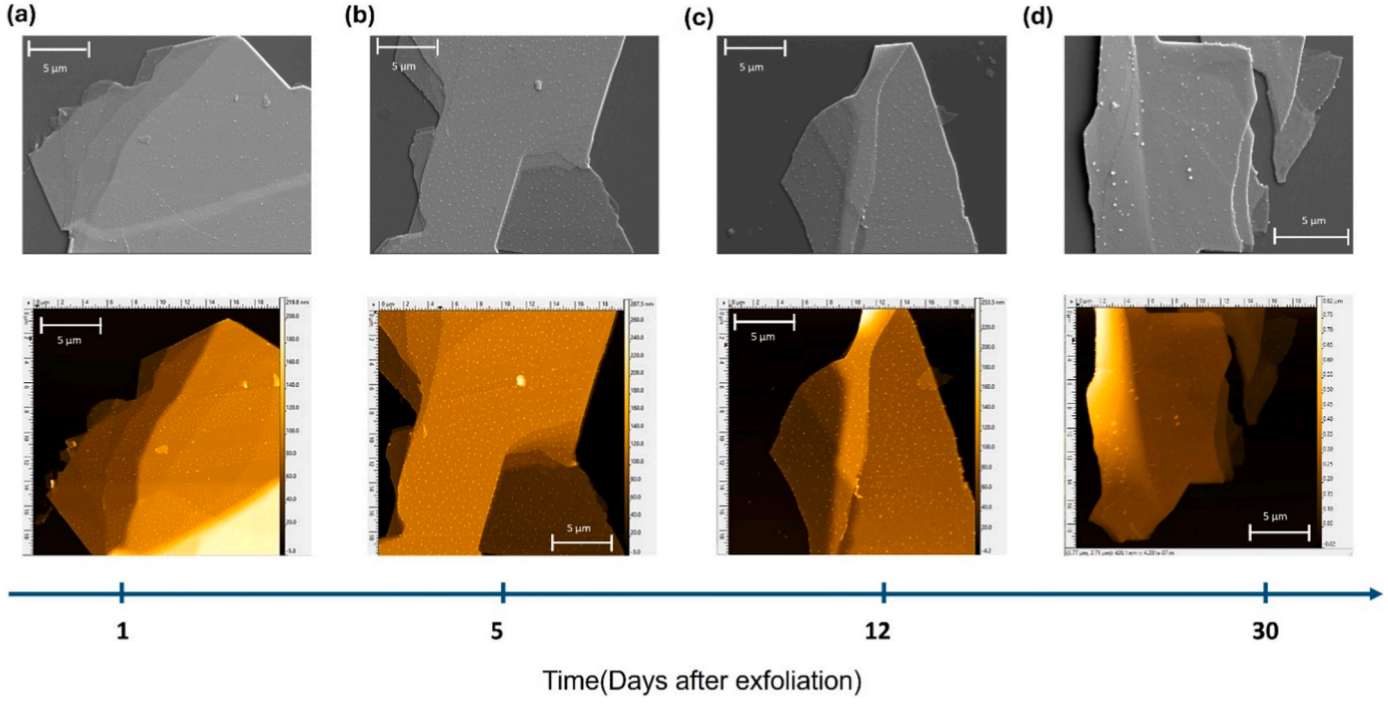

Fig. 2. Time evolution of $ZrSe_2$ surface modification under ambient condition. SEM (top) and AFM (bottom) images of flakes (a) one, (b) five, (c) twelve and (d) thirty days after exfoliation.

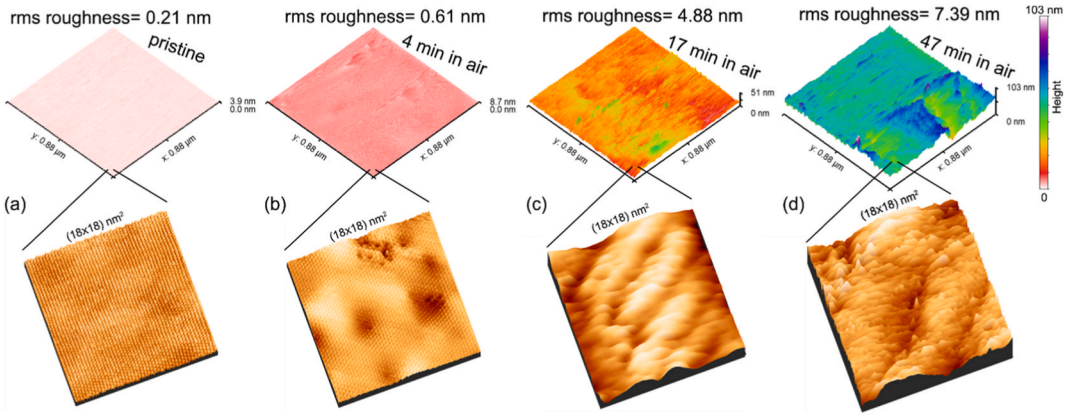

Fig. 3. Atomic-scale evolution of $ZrSe_2$ surface under ambient conditions. (Top panels) 3D STM topographic images illustrating the evolution of surface roughness following incremental air exposure durations. a–d: freshly cleaved $ZrSe_2$ crystal in UHV, and the same sample after 4, 17, and 47 min of air exposure, respectively. All images are presented with the same height scale; the corresponding height ranges and root-mean-square (RMS) roughness values are noted. (Bottom panels) STM images showing 18 × 18 nm^2 zoom-ups of the surface in each condition. STM scanning parameters: (a) V = −1.0 V, I = 40 nA; (b) V = −0.5 V, I = 21 nA; (c) V = −3.9 V, I = 4.7 nA; (d) V = −3.8 V, I = 4.0 nA.

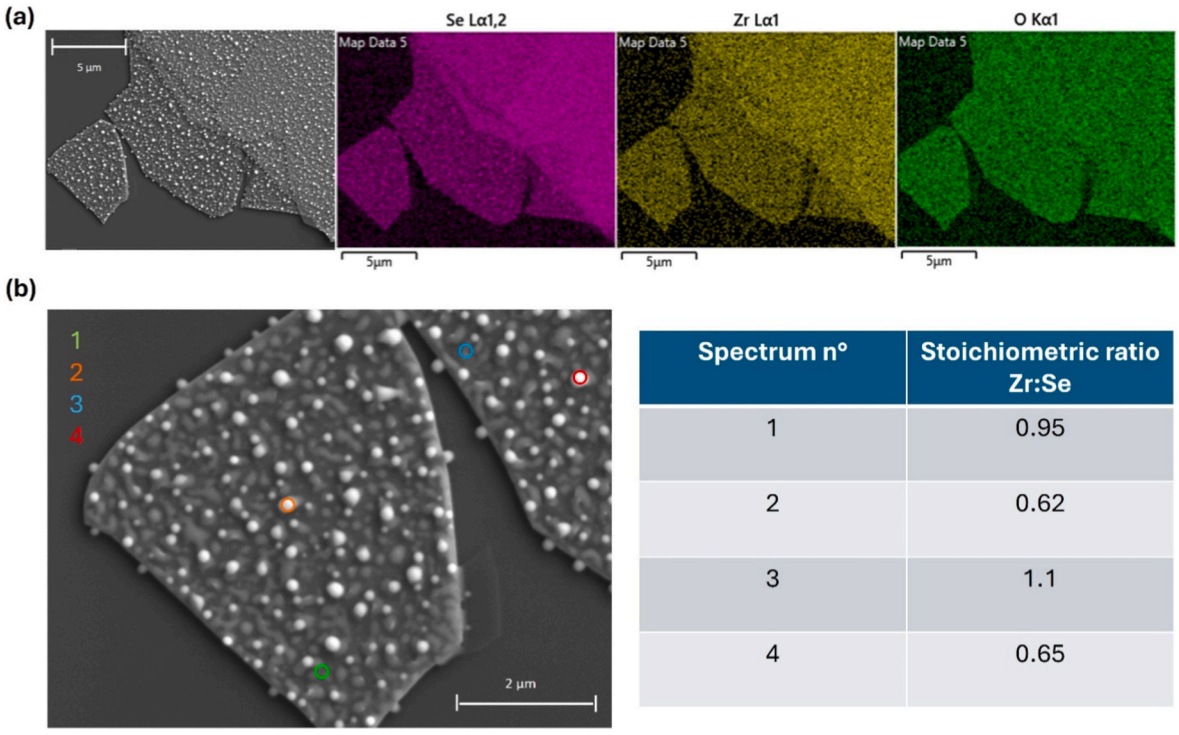

Spectrum n°	Stoichiometric ratio Zr:Se
1	0.95
2	0.62
3	1.1
4	0.65

Fig. 4. Se segregation and blister formation in aged $ZrSe_2$. (a) EDX elemental maps (Se, Zr, O) of a $ZrSe_2$ flake one month post-exfoliation, showing Se-rich blisters and surface modifications. (b) EDX point spectra confirm Se enrichment in protrusions and Se depletion in nearby regions (Zr:Se ≈ 1.1), indicating chemical inhomogeneity from oxidation-driven Se displacement and ZrO_2 formation.

To understand the chemical composition of the features on the $ZrSe_2$ surface, multiple aged flakes were analysed using EDX. Fig. 4a shows a thin 1-month-old flake, in which two distinct features can be observed: localized hemispherical blisters of different dimensions and planar surface modification that might be the initial stage of the formation of the protrusions. They grow both on the surface and laterally from the edges and have diameters up to ~300 nm. Oxidation-induced surface deformations have been observed in other materials [6,16]. EDX maps of the flake showing the spatial distribution of Zr, Se and O, reveal Se segregation. Oxygen likely causes the displacement of Se atoms to form ZrO_2. Similar mechanisms have been reported in previous works for other materials [35]. Se migration is supported by EDX point spectra acquired from several protrusions and protrusion-free areas - see Fig. 4b. The concentration of Zr and Se is almost the same far from the protrusions, as shown by the spectra 1 and 3. This confirms that the sample becomes chemically inhomogeneous after prolonged oxidation.

The oldest flakes, such as the 4-month-old samples shown in Fig. 5, exhibit this mechanism even more clearly. The largest hemispherical protrusions reach diameters of approximately 500 nm. As the oxidation process proceeds, densely-packed groups of protrusions appear to coalesce into a single, larger one, leaving a smoother, flatter area surrounding them. These results highlight that the process is not self-limiting, and that Se aggregation occurs readily at room temperature without any external stimulus. EDX maps confirm the absence of both Zr and O at the protrusions, as highlighted by the triangular shapes in Fig. 5a. EDX spectra collected on the oldest flakes confirm a non-uniform

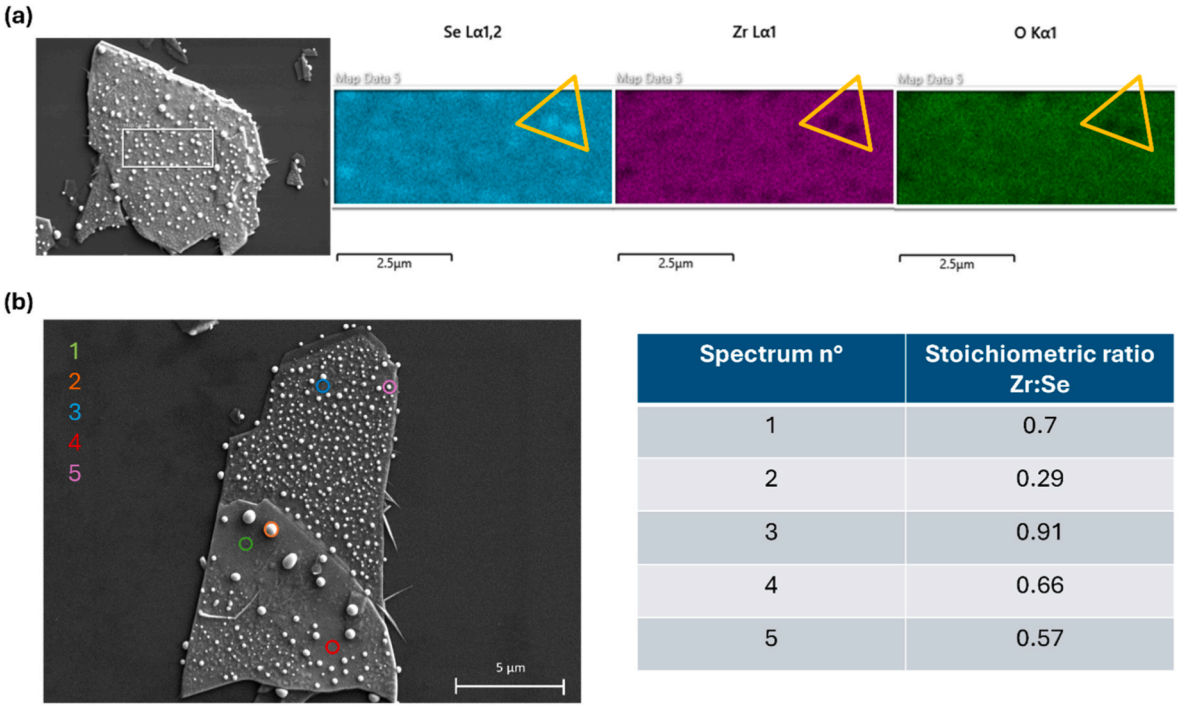

Spectrum n°	Stoichiometric ratio Zr:Se
1	0.7
2	0.29
3	0.91
4	0.66
5	0.57

Fig. 5. Enhanced Se aggregation and nanowire formation in aged $ZrSe_2$. (a) EDX elemental maps (Se, Zr, O) of a flake aged 4 months, showing large Se-rich protrusions (~500 nm) and Se redistribution due to prolonged air exposure. (b) EDX point spectra from blistered and flat regions reveal strong Se enrichment (Zr:Se as low as 0.29) at blisters, indicating significant chemical inhomogeneity. Nanowire formation is also observed in aged samples.

distribution of the chemical species. The Zr:Se stoichiometric ratio ranges from 0.7 to 0.91 on bubble-free regions and from 0.57 to 0.29 on them – see the Table in Fig. 5b. Additionally, aged flakes - such as the one shown in Fig. 5b, also reveal that Se not only grows in the form of protrusions, but also forms nanowires.

Furthermore, Fig. S14b shows the morphology of the flake in Fig. 5a after a 20-min continuous SEM scan, confirming that SEM can alter the surface even after oxidation occurs and demonstrating that it causes a redistribution of selenium atoms through interaction with the electron beam [36].

Cross-sectional EDX was performed normal to the flake surface from the top of the protrusion deep into the Si/SiO_2 substrate. Fig. 6a and b show an SEM image of a $ZrSe_2$ flake with the approximate location of FIB lamella extraction highlighted, and the FIB-SEM cross-section image of the $ZrSe_2$ flake on Si/SiO_2, respectively. Looking at Fig. 6c, from left to right, we have the Si substrate, then the 85 nm thick SiO_2 that appears as a dark region, the $ZrSe_2$ flake and the protrusion on top of it. The oxygen concentration is at its maximum at the interface between the SiO_2 and the flake, and then it decreases. The Zr concentration is at its maximum in correspondence with the flake, but only a low amount is detected in the protrusion, which is predominantly made of Se, as expected. Two peaks can be identified in the Se spectrum, one in correspondence with the flake and the other at the centre of the protrusion.

A Focused Ion Beam (FIB) cross-section of a protrusion was measured in a Tescan Tensor 4DSTEM system with correlated EDX operated at an accelerating voltage of 100 kV and a probe current of 1 nA. The convergence angle was 9.78 mrad. The cross-section region and lamella survey are shown in Fig. 6d and e. During the measurement of the protrusion, voids began to form in the lamella, necessitating a reduction of the beam current to 500 pA, which stabilized the sample. Fig. 6d shows the structure of the protrusion and underlying flake. The protrusion is embedded in a ZrO_2 layer measuring 20–50 nm which extends beneath the protrusion, separating it from the underlying $ZrSe_2$. The $ZrSe_2$ layer exhibits phase separation into alternating layers of Se-rich and Se-depleted regions. The dark band at the surface is composed of almost pure Se, while the bright voids are composed of almost pure ZrO_2. The darker central region is well mixed, with a Zr:Se ratio of ~20:50, making the flake slightly Se-rich. A thin layer of carbon, less than 5 nm thick, resides between the substrate and $ZrSe_2$ flake, which is likely a residue from the transfer process. Since the ZrO_2 layer extends beneath the protrusion, this indicates the blister formed on top of the oxide, not through it - suggesting the Se blister may have formed as a consequence of Se segregation from the $ZrSe_2$ due to oxidation. The formation of a native ZrO_2 layer on $ZrSe_2$ has previously been observed [7] as has the segregation of Se as a consequence of oxidation [21]. Se poorly wets oxide substrates at room temperature, which can lead to the formation of blisters in selenium melts. The segregated Se near the ZrO_2 layer may therefore have spontaneously aggregated into blisters on the surface oxide [37].

As shown in Fig. 7a, aged flakes reveal that selenium not only accumulates as hemispherical protrusions but can also spontaneously self-assemble into nanowires, with widths reaching up to ~100 nm. The FIB cross-section of the flake in Fig. 7a, presented in Fig. 7b, shows two such nanowires embedded in the structure. These nanowires are coated with a thin carbon layer, although distinguishing it from the surrounding e-beam deposited platinum - used to protect the sample during FIB processing - is challenging (see Fig. 7c–e). Interestingly, the nanowires have etched into the underlying SiO_2 substrate. However, this is not due to reduction processes, as they contain negligible oxygen (Fig. 7c). Instead, EDX point scans confirm that the wires are composed of pure Se, as further demonstrated in Fig. 7d and e. Their high crystallinity, supported by structural data in Fig. S15, suggests that these nanowires result from a spontaneous growth mechanism during ageing.

The nanowires emerging from the flake in Fig. 7f were captured through AFM-see Fig. 7g. The AFM profile in Fig. 7h indicates that the maximum diameter of the nanowires protruding from the substrate is around 44 nm, while it reaches up to 124 nm for those lying flat on the surface, as reported in Fig. 7i. Additionally, their lengths range from a few microns up to 10–15 μm, as observed in representative flakes in Fig. S16, enabling us to identify them as 1D Se nanostructures, opening a new area of investigation. A statistical analysis of the blister sizes and nanowire lengths is provided in Section S.8.

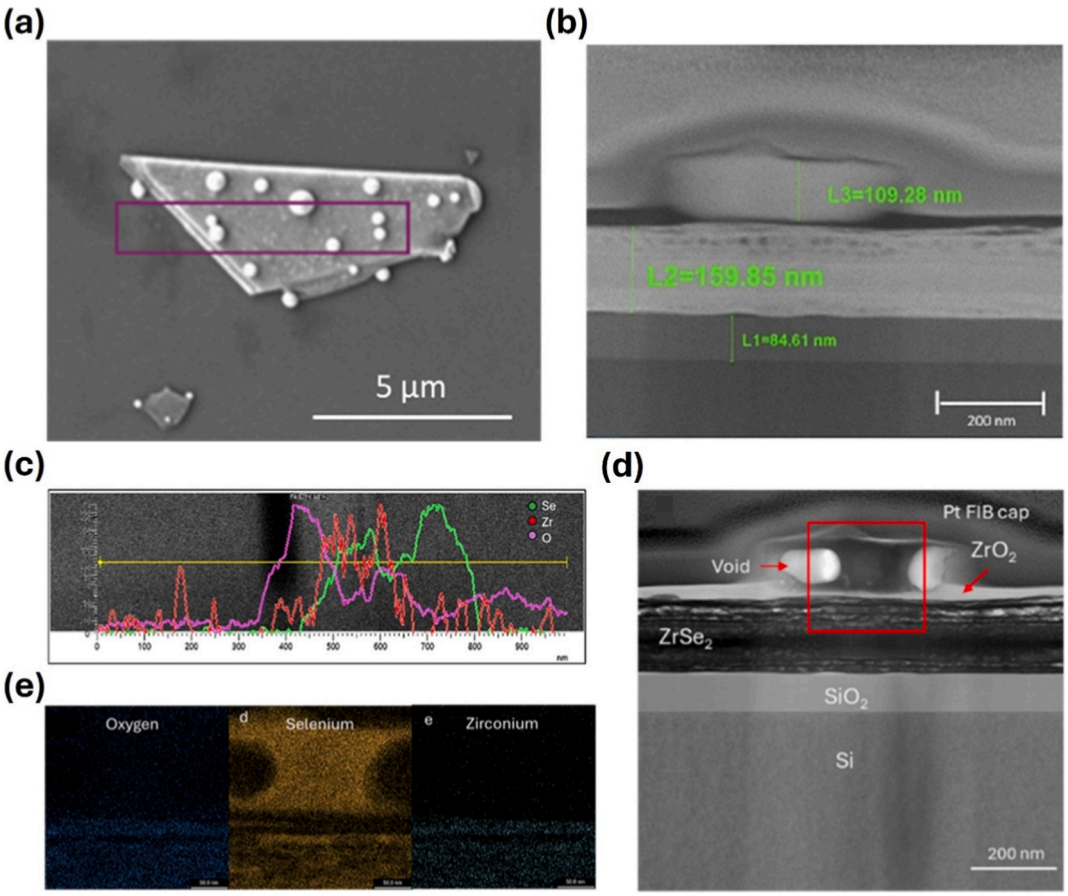

Fig. 6. Cross-sectional STEM and EDX analysis of blisters. (a) SEM image of $ZrSe_2$ flake with the approximate location of the FIB lamella extraction highlighted. (b) FIB-SEM cross-section image of the $ZrSe_2$ flake on a Si/SiO_2 substrate. (c) Cross-sectional EDX line spectra, showing elemental distribution across the substrate, flake, and protrusion. (d) STEM survey image of the large protrusion and underlying layers. The red box highlights the region where correlated EDX was recorded. (e) Correlated EDX maps of the protrusion, showing strong Se segregation. (For interpretation of the references to colour in this figure legend, the reader is referred to the Web version of this article.)

Considerable research has focused on synthesizing Se-based nanostructures such as nanowires, nanotubes, and nanorods, given selenium's intriguing physical properties - notably high photoconductivity, piezoelectricity, thermoelectricity, and nonlinear optical responses [38]. Se exists in several allotropic forms, including trigonal, monoclinic, and amorphous phases. Of these, the trigonal structure is thermodynamically the most stable, and its chain-like configuration naturally supports 1D anisotropic growth [39].

Se nanowires are typically grown from precursor solutions or solid compounds [40,41]. They can be synthesized using various methods - for instance, by dispersing amorphous selenium (a-Se) nanoparticles in ethanol and storing them in the dark at room temperature, which gradually dissolves the a-Se and leads to the formation of trigonal Se (t-Se) seeds and eventually t-Se nanowires. According to the literature, an alternative approach involves dispersing the nanoparticles in water and heating them to 85 °C. A modest temperature increase is sufficient to trigger the amorphous-to-trigonal phase transition, given its relatively low transformation energy of only 6.63 kJ/mol [42]. SEM images of several aged flakes suggest that Se nanowire growth initiates at Se-rich protrusions - both at the flake edges and across the surface. Fig. S16a and S.16b show how nanowires can extend from multiple protrusions and merge into longer continuous structures.

As further discussed in the following section, identifying the phase of Se in the hemispherical protrusions is challenging. We tentatively assume it to be amorphous, as these features result from air exposure-induced oxidation. However, the tubular morphology of the nanowires and the diffraction pattern in Fig. S15 suggest that they adopt a trigonal phase. This transition is likely favoured by the lower surface energy of t-Se compared to a-Se [43]. Thus, the formation of Se nanowires from oxidized $ZrSe_2$ warrants deeper investigation, with the aim of enabling controlled growth and the exploitation of their intrinsic properties [44,45].

The growth of nanowires appears to be a gradual process, typically requiring 3–4 months. To accelerate the Se phase transition, we annealed several aged flakes (exfoliated on Si and Si/SiO_2) in air at 200 °C for 1 h. This temperature is sufficient to promote Se evaporation [46], as confirmed by SEM and EDX. However, Raman spectra indicated that Se was not completely removed, suggesting that residual atoms may crystallize into trigonal nanocrystals - thereby accelerating nanowire nucleation [22]. A comparison of pre- and post-annealed flakes is shown in Fig. S18. This result suggests that controlled annealing of aged flakes could serve as a viable method for oxidizing $ZrSe_2$, although further study of the resulting surface ZrO_x layer is needed to determine its structure and quality.

3.3. Phase evolution and chemical modification

Raman spectroscopy provides further insights into how the oxidation process evolves over time. $ZrSe_2$ flakes were mechanically exfoliated onto a p^+-Si/SiO_2 substrate, and the Raman spectrum was acquired multiple times over a month on the same flake, only changing the location of the laser spot. During this period, the sample was stored in the cleanroom environment.

$ZrSe_2$ presents a 1T structure with a P-3m1 space group and the unit

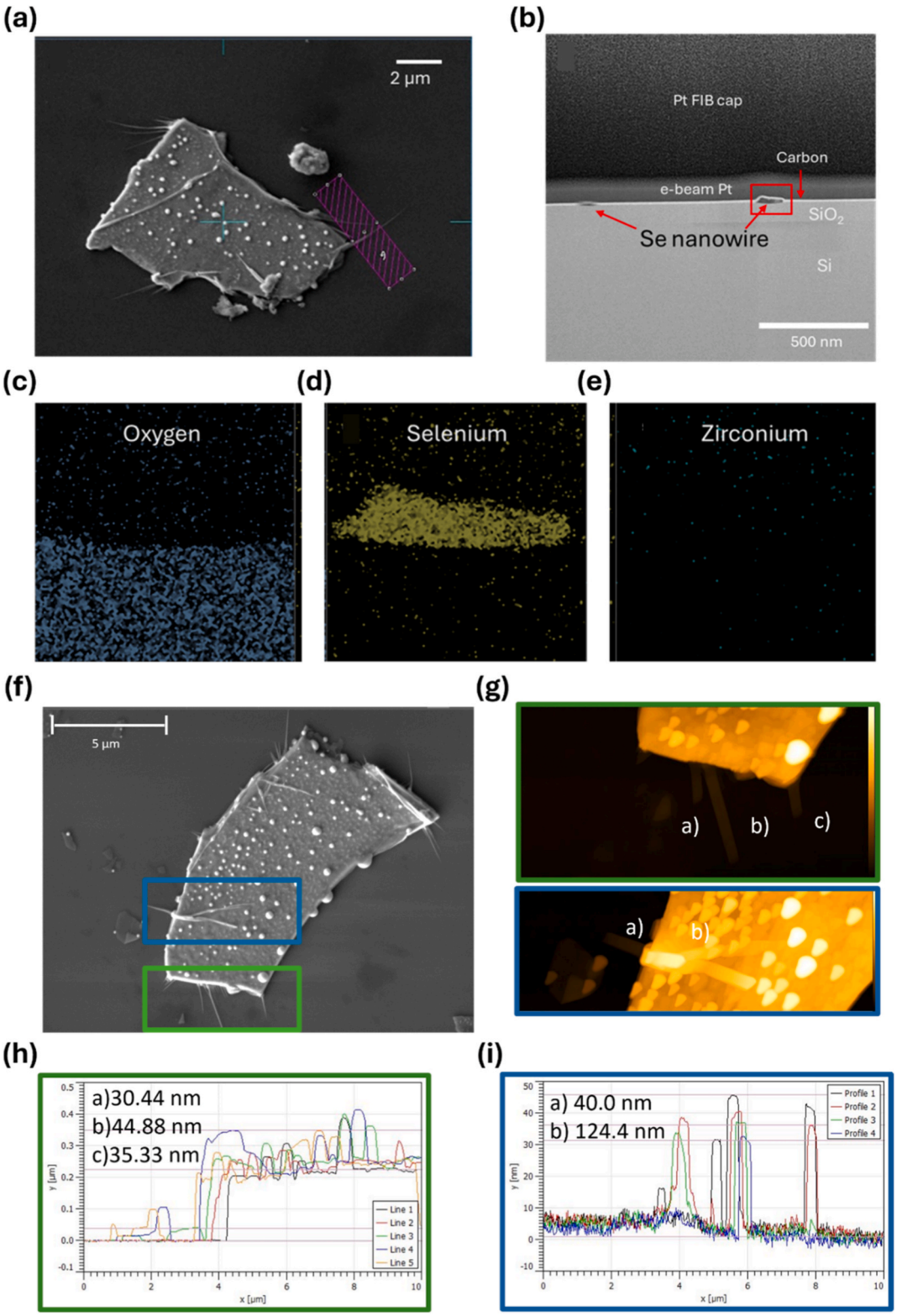

Fig. 7. Spontaneous formation of Se nanowires on aged $ZrSe_2$ Flakes. (a) SEM image of an aged $ZrSe_2$ flake showing surface nanowires, with the FIB lamella extraction region marked in purple. (b) STEM cross-sectional image highlighting two Se nanowires embedded in the flake structure. (c–e) EDX elemental maps confirming the nanowires are composed of pure Se with negligible oxygen or zirconium content. (f) SEM image of another aged flake displaying nanowires, with AFM scan regions outlined. (g) AFM topography images of selected regions. (h–i) AFM profiles showing the height and width of nanowires. (For interpretation of the references to colour in this figure legend, the reader is referred to the Web version of this article.)

cell is given by $\alpha = \beta = 90°$, $\gamma = 120°$ and $a = b = 3.772(2)$ Å, $c = 6.1258(5)$ Å. The Raman spectrum acquired immediately after exfoliation is shown in Fig. 8a. A small peak corresponding to the in-plane mode E_g appears at (145.3 ± 1.7) cm^{-1} and a sharp one, associated with the out-of-plane A_{1g} mode, is visible at (193.51 ± 0.03) cm^{-1}. These values are consistent with the ones reported in literature [47]. In addition, we detect the IR-active modes E_u, around 211 cm^{-1} and the A_{2u} at (261 ± 2) cm^{-1} [48,49].

Fig. 8b shows the spectra acquired at 1, 2, 5, 8, 12, and 30 days after exfoliation. Over the first 12 days, both E_g and A_{1g} $ZrSe_2$ peaks are clearly visible, and no significant shift is observed. The A_{2u} peak, normally located around 261-264 cm^{-1} in fresh exfoliated flakes, is replaced by a broad peak around 253 cm^{-1} that gradually increases over time (see Section S.10 for more details). After one month, the E_g and A_{1g} are no longer detectable. The top spectrum, also shown in Fig. 8c, displays only a peak besides the Si peak, which we attribute to likely amorphous Se (a-Se) [49,50]. This assignment is consistent with the formation of blisters through a spontaneous aggregation process, where an initially amorphous structure is expected. This result further confirms the nature of the hemispherical protrusions described in the previous section. The disappearance of the $ZrSe_2$ peaks after a certain period, which likely depends on the thickness of the flake, reveals that the exposure to air dramatically and irreversibly modifies the chemical structure of the material.

It is not straightforward to identify the precise structure of Se through Raman spectroscopy. As mentioned above, the two principal crystalline Se allotropes are the trigonal form (t-Se), consisting of ordered polymeric Se_n chains, and the monoclinic Se (m-Se) with ordered Se_8 rings. However, the structural parameters of these two phases are so similar that Raman spectroscopy itself can induce a photo- and heat-driven ring-to-chain transition. To minimize this effect, above-bandgap excitation lasers with low photon flux and below-bandgap excitation lasers at low temperature are needed [50,51].

Our Raman setup, as described in the methods section, does not fully meet the stringent requirements needed to ensure that photo- or heat-induced transformation in Se is prevented. Based on the collected spectrum, the Se peak, shown in Fig. 8c, can be fitted as an envelope of one weaker peak at (233.9 ± 0.2) cm^{-1} and a more distinct one at (253.45 ± 0.05) cm^{-1}. The first peak might be attributed to the bond-stretching vibrational mode of ordered Se chains in t-Se, which typically occurs at 236 cm^{-1}, while the second corresponds to the bond-stretching vibrational mode of Se rings [46]. Raman spectroscopy thus confirms the Se-rich nature of the blisters and suggests that they may be a mixture of ordered chains and disordered rings, but additional structural analyses would be required for confirmation.

The spectra were acquired again two months later, varying the absolute power from 0.175 to 0.7 mW (corresponding to 0.25–1 % of the nominal laser intensity), as reported in Fig. 8d, over the 100-500 cm^{-1} range. The two Se peaks are clearly visible and well separated, the first one located around 234-235 cm^{-1} and the other one around 252-253

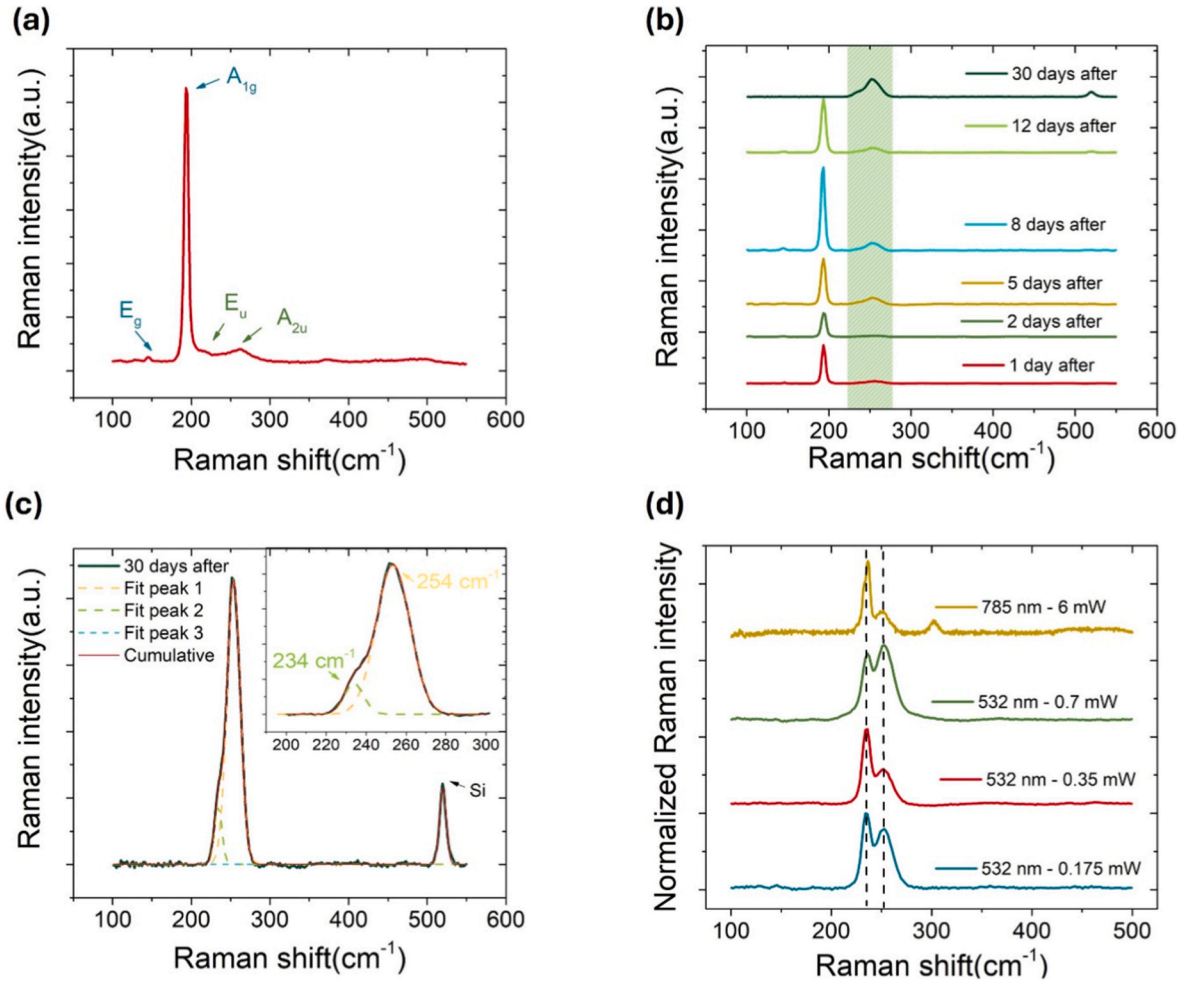

Fig. 8. Time evolution of $ZrSe_2$ Raman spectra during ambient air exposure. (a) Raman spectrum of freshly exfoliated $ZrSe_2$ showing E_g, A_{1g}, E_u, and A_{2u} modes. (b) Raman spectra acquired at multiple time points over 30 days; the shaded region highlights the emerging broad peak. (c) Spectrum after 30 days, showing the disappearance of $ZrSe_2$ modes and the appearance of a Se peak; inset: peak fitting reveals contributions at 234 and 254 cm^{-1}. (d) Raman spectra after 3 months acquired at different excitation wavelengths and powers.

cm^{-1}. The relative intensities of the two peaks change with laser power, in agreement with previous reports in the literature. The response was also analysed under a below-bandgap excitation laser (785 nm), which required a higher power intensity of 6 mW. The spectrum shows a peak at (235.6 ± 0.2) cm^{-1} and the other one at (251.9 ± 0.9) cm^{-1} where the 251 nm peak is associated with a disordered chain structure. A spectral profile similar to that reported in Fig. 8c was also observed at several intensities on other flakes on the same chip. However, for the reasons discussed above, these results cannot be considered conclusive about the nature of selenium within the blisters.

3.4. Chemical status of the exposed $ZrSe_2$ surface

Fig. 9 presents high-resolution XPS spectra of the Zr 3*d* and Se 3*d* core levels for a freshly exfoliated $ZrSe_2$ surface, compared with the same flake after 1 h of air exposure. Prior to exfoliation, the as-received bulk crystal already shows surface oxidation, as indicated by the XPS data in Fig. S19. This spectrum reveals the presence of zirconium oxide (Zr-O), along with signals corresponding to elemental selenium (Se-Se). Notably, the core-level peaks in the as-received sample are shifted by ~1.0 eV to higher binding energy (BE) due to the formation of native ZrO_2. In contrast, the surface of the freshly exfoliated crystal is dominated by the Zr-Se chemical state, as detected in both the Zr $3d_{5/2}$ and Se 3*d5/2* spectra at BE positions of 181.2 eV and 53.8 eV, respectively [52]. A secondary chemical state in the Zr 3*d* spectrum appears at 182.5 eV, attributed to Zr-O [53], indicating minor oxidation even though exfoliation was performed under an N_2 atmosphere. A small Zr 4*s* peak is also observed at 52.4 eV [54]. After 1 h of exposure to ambient air, further oxidation is clearly evident from the increased intensity of the Zr-O peak. Additionally, the Se 3*d* spectrum displays a new peak at BE of 54.9 eV, associated with the formation of Se-Se compound [55]. These XPS results are consistent with the EDX analysis, which reveals Se-rich blisters on the oxidized ZrO_2 surface.

3.5. Theoretical insight into Se segregation via DFT simulations

To provide further insight into the experimental observation of Se-rich protrusions and nanowire formation, we performed density functional theory (DFT) calculations modelling the early and advanced stages of oxidation on $ZrSe_2$. The simulations consider increasing concentration of oxygen atoms adsorbed into a $ZrSe_2$, representing the progression of ambient exposure. The simulation results are illustrated in Fig. 10, which shows how oxygen incorporation leads to progressive Se detachment and clustering.

Our DFT simulations show that oxygen atoms preferentially adsorb onto undercoordinated Zr atoms, especially at edge sites and surface defects. This leads to a progressive weakening and eventual breaking of nearby Zr-Se bonds. The simulations indicate that as oxygen concentration increases, oxygen penetrates the top layers of $ZrSe_2$, forming Zr-O bonds and destabilizing the Zr-Se lattice. These effects emerge at relatively low oxygen coverage, consistent with our experimental observation that degradation begins within seconds to minutes of ambient air exposure (see STM results in Section 1 and XPS data in Section 4).

Under extended oxidation, detached selenium atoms migrate across the surface and cluster atop or near the ZrO_2 regions, consistent with the poor wettability of Se on oxides and the phase-separated structures seen in cross-sectional TEM and EDX analysis. Our simulations show the emergence of stable Se-Se bonds, supporting this clustering behaviour.

These findings correlate with our experimental results, where hemispherical Se blisters and nanowires were observed via AFM, SEM, STM, and STEM. Experimentally, we observe Se-rich protrusions (blisters) forming as early as 3 h post-exfoliation (Fig. 1d), with a significant increase in density and size after 1 day (Fig. 2a). Over longer periods (1–4 months), these features evolve into larger aggregates and eventually Se nanowires (Figs. 5 and 7). Thus, the Se clustering begins within hours and continues progressively over weeks to months.

3.6. Encapsulation strategy: suppressing oxidation and preserving material's integrity

The previous sections highlight that preventing or limiting the degradation process is critical for $ZrSe_2$, both for fundamental studies and for device fabrication. To address this, we propose an encapsulation strategy as follows. As mentioned in the Methods section, after exfoliating $ZrSe_2$ flakes on Si/SiO_2 (85 nm) substrates in a glovebox, a ZrO_2 film (2 nm nominal thickness) was e-beam evaporated to encapsulate the samples. Air exposure is limited to 40 s solely to mount them in the evaporator. We chose ZrO_2 because it minimizes compatibility issues between the semiconductor and the dielectric layer, as both materials share Zr as a constituent.

The reliability of the process is initially evaluated by AFM measurements performed two months after encapsulation on multi-stepped flakes. AFM images, reported in section S.12, do not show any appre-

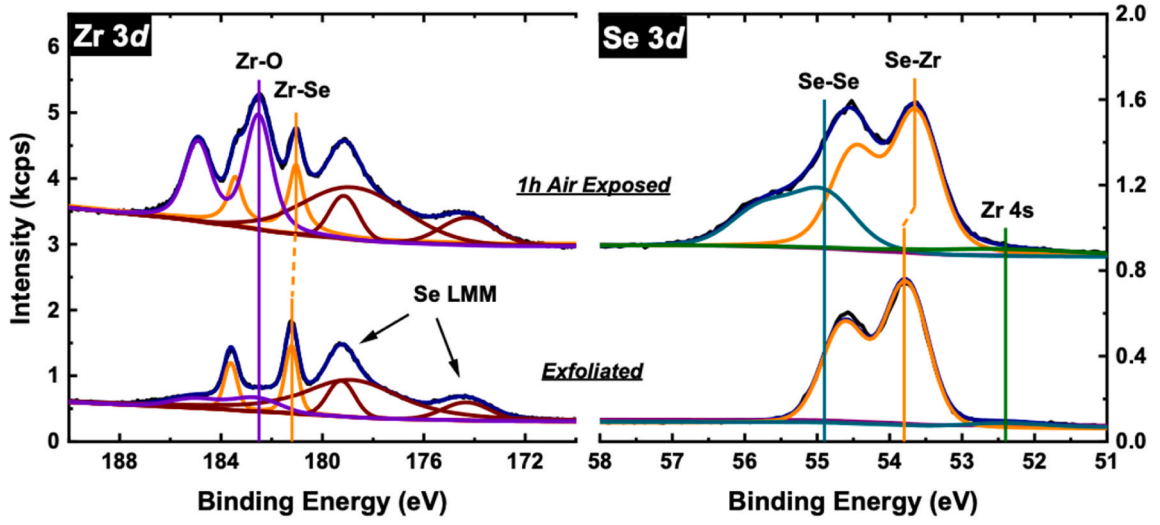

Fig. 9. Surface chemical evolution of $ZrSe_2$ upon air exposure. High-resolution XPS spectra of Zr 3*d* and Se 3*d* core levels in bulk $ZrSe_2$ comparing a freshly exfoliated flake and the same flake after 1 h of air exposure. The Zr 3*d* core level overlaps with Se LMM Auger peaks.

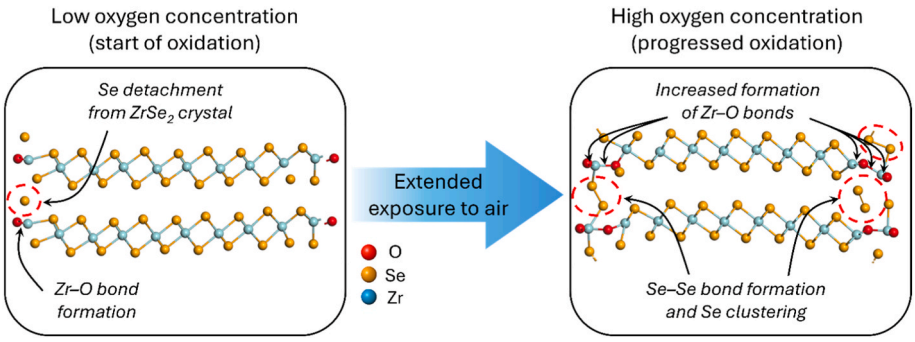

Fig. 10. DFT simulation of oxidation progression in $ZrSe_2$. Density functional theory models showing how oxygen incorporation disrupts Zr-Se bonds, resulting in the progressive detachment and clustering of Se atoms. Left: initial stage with low oxygen concentration showing Zr-O bond formation and Se atoms beginning to displace. Right: advanced stage with higher oxygen concentration forming Se-rich clusters detached from the $ZrSe_2$ lattice.

ciable signs of degradation in the regions thicker than ~ 12 nm. However, the higher density of protrusions observed in thinner flakes ($\lesssim$ 6 nm) is likely due to their brief exposure to air prior to encapsulation, which is more critical for thin layers because of their higher surface-to-volume ratio and the greater presence of structural defects and edge sites. Moreover, possible incomplete coverage of the flake edges by the ZrO_2 layer, along with structural imperfections in the oxide, facilitates oxidation throughout the entire thickness, unlike in thicker flakes. AFM on encapsulated flakes helps in qualitatively linking the thickness of the $ZrSe_2$ flakes to their apparent colour on 85 nm of SiO_2 under optical microscopy, which is a useful way to rapidly identify thin flakes – see Fig. S21.

Raman spectroscopy, also performed a couple of months after fabrication, provides more quantitative and precise information than AFM. Raman spectra reveal signal from $ZrSe_2$ regions of different thickness. To have a visual understanding of the situation, some spectra are displayed in Fig. 11, while the whole set of data is collected in Fig. S22 and S23. The parameters extracted for the peaks are reported in Table S2. The thickness values reported in the respective column include the ZrO_2 layer thickness. For flakes with a thickness $\gtrsim$ 4.42 nm, both E_g and A_{1g} mode are detected. In contrast, A_{1g} peak alone is visible for the 4.11 nm thick flake, and neither of the two peaks can be identified for the 3 nm-thick flake [18]. The oxidation status of the different parts can be qualitatively identified by examining the A_{2u} peak, as previously asserted. Focusing on the position of the peak, we observe a transition from the A_{2u} to the Se peak, as the thickness of $ZrSe_2$ decreases and the respective degradation increases. Precisely, the additional peak, highlighted by a blue arrow in Fig. 11a, is found at ~ 262–264 cm^{-1} in regions thicker than 6 nm. At the critical thickness of 6 nm, it shifts to ~ 260 cm^{-1}, and for thinner flakes, it further shifts to ~ 252–254 cm^{-1}.

Fig. 11b, on the other hand, displays the peaks' height of the two vibrational modes as a function of the thickness of the flake. The peaks' intensity does not have a monotonic behaviour but instead shows a peak-shape profile. Moving from 115 nm down to thinner flakes, it increases, reaching a maximum for ~ 8 nm thick flakes, and then it decreases again until the peaks are not detectable anymore. Moreover, Raman signal of bulk $ZrSe_2$ is weaker than that of 4.42 nm thick flake. This nonmonotonic dependence of Raman intensities on the sample thickness has been previously observed in graphene [56] and in other TMDs, like MoS_2 [57], $TaSe_2$ [58], and others [59]. It is attributed to optical interference effects arising from multiple reflections of both the excitation laser and the emitted Raman signal within the material, at the upper interface, and at the SiO_2 substrate. The presence of the oxide layer on top of the silicon substrate leads to optical field enhancement, which strengthens the Raman signal of thinner flakes and results in a peak when constructive interference occurs.

3.7. *$ZrSe_2$-based field-effect transistor*

As described in the Methods section, back-gated field effect transistors (FETs) were fabricated by depositing Cr/Au (15/150 nm) contact leads by e-beam evaporation on $ZrSe_2$ flakes exfoliated on Si/SiO_2 (85 nm) substrates and encapsulated with a 2 nm thick ZrO_2 layer. The encapsulation layer is expected to act as a thin tunnel barrier for charge

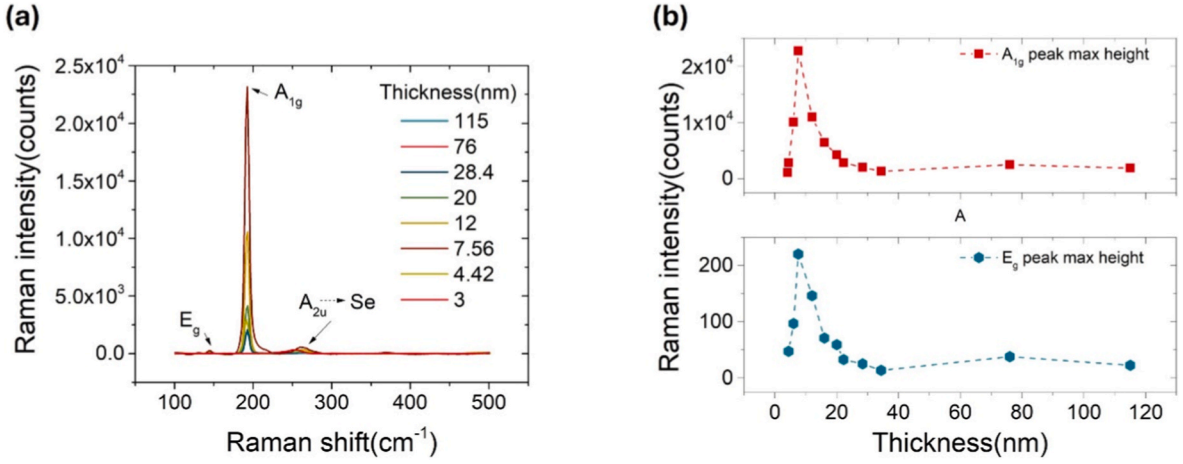

Fig. 11. Thickness dependence of $ZrSe_2$ Raman modes. (a) Raman spectra of $ZrSe_2$ flakes with varying thicknesses (3–115 nm), showing the evolution of the E_g and A_{1g} peaks. (b) Maximum intensity of A_{1g} (top) and E_g (bottom) Raman peaks as a function of flake thickness, extracted from the spectra in (a). Both modes exhibit strong thickness-dependent behaviour.

injection between the metal contact and the $ZrSe_2$ flakes. The schematic of the device, along with the measurement setup, is depicted in Fig. 12a. Drain current vs. drain voltage (I_{ds}-V_{ds}) and drain current vs. gate voltage (I_{ds}-V_{gs}) measurements were performed at room temperature in the dark.

The inset of Fig. 12b shows the optical image of one of the devices with a channel length of L ~ 2.5 μm and a width of W ~ 7.5 μm. The I_{ds}-V_{ds} characteristic in Fig. 12b shows an asymmetric behaviour, with a maximum current of about 1 μA at $V_{ds} = 1$ V, suggesting a Schottky-like behaviour at the metal contacts [60,61]. Fig. 12c presents the output curves, obtained by sweeping V_{ds} from −1 to 1 V and stepping V_{gs} from −40 to 40 V. Positive gate biases result in a higher current compared to the negative ones, indicating n-type conduction in $ZrSe_2$, despite the weak gate dependence. The n-type current transport is further confirmed by the transfer curve in Fig. 12d, obtained by double sweeping the gate bias from 40 to −40 V at a fixed $V_{ds} = 0.5$ V. The gate current is in the order of pA, which indicates that there is no gate leakage. A relatively high mobility of $\mu = (1.67 \pm 0.17)$ $cm^2\ V^{-1}\ s^{-1}$, comparable with other works on $ZrSe_2$ [7], is calculated by the slope of the linear fit of the upper part of the transfer curve at positive biases, using the following formula:

$$\mu = \frac{L}{(C_{ox}\ V_{ds}\ W)}\left(\frac{dI_d}{dV_{gs}}\right)$$

where C_{ox} is the oxide capacitor per unit area ($C_{ox} = 4.06 \times 10^{-8}$ F/cm^2). Despite this result, the device exhibits a limited I_{on}/I_{off} ratio and a pronounced hysteresis. These effects can be attributed to intrinsic defects in the $ZrSe_2$ flake, and to the defective interfaces with both SiO_2 substrate and ZrO_2 encapsulation layer [62,63]. The inhomogeneous potential landscape usually associated with non-ideal semiconductor/SiO_2 interface in terms of roughness, along with the presence of trapped charges at the semiconductor/dielectric interface can degrade the device performance and compromise electrostatic control [64]. Moreover, damage induced by emitted electrons and ions during evaporation of ZrO_2 onto the material surface may have introduced additional surface defects [65]. Finally, the charge injection mechanism through the encapsulating layer at the metal contacts may also limit overall device performance.

These results underscore the need to address material and interface quality issues. To achieve these objectives, several strategies can be considered while maintaining the transistor structure presented in this section. These include performing the entire fabrication process in an inert glovebox to prevent air exposure, enabling the safe use of few-layer flakes, which is beneficial for improving gate control and current modulation. Additional improvements involve optimizing ZrO_2 deposition parameters to reduce interface damage, exploring alternative gate dielectrics such as hexagonal boron nitride (hBN) to minimize charge trapping [66], and refining contact geometry to enhance charge injection and overall device stability.

By refining the fabrication process and interface quality, $ZrSe_2$-based FETs have the potential to reach performance levels comparable to those of well-established 2D semiconductors, as their unoptimized mobility is already relatively high. For comparison, MoS_2 in similar devices exhibits mobilities ranging from less than one tenth to a few dozens, I_{on}/I_{off} ratios of 10^5–10^8, and subthreshold swings (SS) of few V/decade [67].

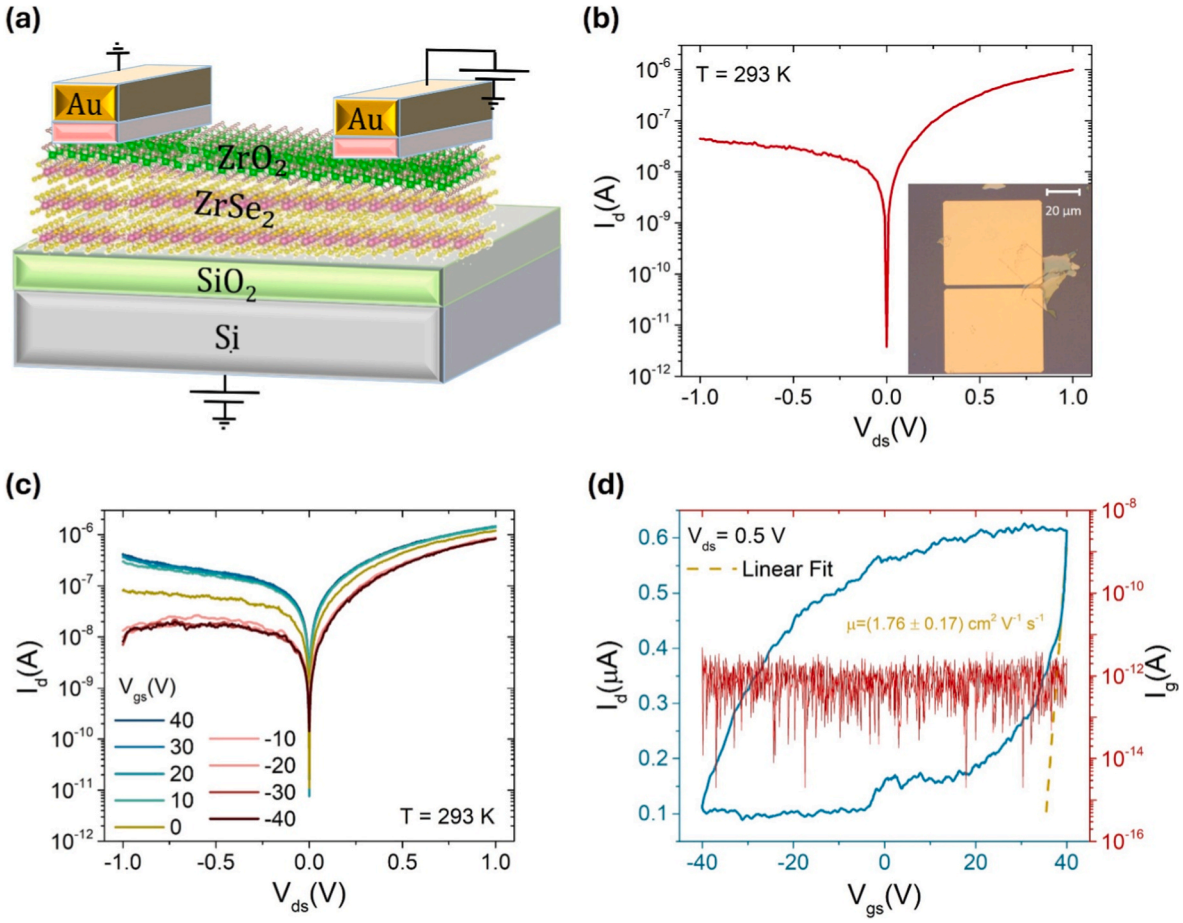

Fig. 12. Back-gated $ZrSe_2$ FET device. (a) Schematic illustration of the $ZrSe_2$ FET with the electrical measurement set up. (b) I_{ds}-V_{ds} characteristic measured in the dark at room temperature. The inset shows the optical image of the device, with a channel length of ~2.5 μm. (c) Output curves under different gate voltages. (d) Transfer characteristic at a fixed $V_{ds} = 0.5$ V.

Monolayer WS_2 FETs report mobilities up to ~33 $cm^2/V{\cdot}s$ with similar switching ratios [68], while black phosphorus (BP) can exceed 100 $cm^2/V{\cdot}s$ in mobility but suffers from severe environmental instability [69].

However, as shown in Fig. 6, a key advantage of $ZrSe_2$ is that oxidation naturally forms a native high-κ ZrO_2 layer, a property not shared by MoS_2, WS_2, or BP. This feature directly addresses a central challenge in 2D semiconductor integration: the identification and fabrication of suitable gate dielectrics for practical electronics. In contrast, the native oxides of Mo- and W-based dichalcogenides are typically leaky and unsuitable as dielectrics [70], and BP does not form a stable native oxide. Thus, the ability to obtain a native functional gate dielectric represents a promising integration pathway for $ZrSe_2$. Our findings provide further insight into this mechanism.

4. Conclusions

In this work, we have systematically investigated the air-induced degradation of $ZrSe_2$, revealing that oxidation dramatically alters both the morphology and electronic performance of this promising 2D semiconductor. Through a combination of AFM, SEM, STM, EDX, XPS, Raman spectroscopy, and FIB-TEM, supported by density DFT simulations, we uncover the progressive formation of Se-rich hemispherical blisters and one-dimensional nanowires, arising from selenium segregation triggered by native Zr oxide growth. EDX analysis shows Se enrichment in oxidized domains, Raman spectroscopy tracks the corresponding spectral evolution – disappearance of $ZrSe_2$ peaks and emergence of Se signatures over time, and XPS confirms the formation of Zr-O and Se-Se bonds, providing further evidence for chemical oxidation and selenium segregation. DFT simulations offer mechanistic confirmation that oxygen adsorption weakens Zr-Se bonds, enabling Se detachment and clustering at the surface. We demonstrate that oxidation begins within minutes of air exposure, initially at edge sites - consistent with known TMD oxidation pathways - but rapidly spreads across the basal plane. Protrusions identified via SEM/AFM are composed of Se in mixed trigonal and amorphous phases, as confirmed by Raman and cross-sectional STEM analysis. Over time, smaller blisters coalesce into larger ones (up to 500 nm in diameter), eventually giving rise to Se nanowires up to 10–15 μm long, either protruding from the flake edges or lying atop the surface. These nanostructures form without any external stimulus. Interestingly, repeated SEM imaging was found to inhibit protrusion growth, highlighting the beam's irreversible impact on surface evolution. Our encapsulation strategy using thin e-beam evaporated ZrO_2 offers partial protection, underscoring the need for more robust passivation techniques. Despite the challenges, preliminary FETs fabricated from encapsulated $ZrSe_2$ exhibit n-type conduction and a promising mobility of ~1.7 $cm^2V^{-1}s^{-1}$. This study not only advances the mechanistic understanding of $ZrSe_2$ surface degradation, but also highlights the broader importance of surface chemistry in determining 2D device stability. The insights gained are relevant for a wide range of TMDs, where native oxide formation and chalcogen segregation may both degrade and enable new functionalities in next generation nanoelectronics and optoelectronics.

CRediT authorship contribution statement

Kimberly Intonti: Writing – original draft, Validation, Methodology, Investigation, Formal analysis, Data curation, Conceptualization. **Hazel Neill:** Writing – original draft, Validation, Methodology, Investigation, Formal analysis, Data curation, Conceptualization. **Sharieh Jamalzadeh Kheirabadi:** Software, Methodology, Investigation, Formal analysis, Data curation. **Zabeada Aslam:** Resources, Methodology, Investigation. **Timothy Moorsom:** Visualization, Software, Resources, Methodology, Investigation. **Joslin Sunder Prasanna:** Visualization, Software, Resources, Methodology, Investigation. **Rafik Addou:** Validation, Resources, Methodology, Investigation. **Luca Persichetti:** Validation, Software, Resources, Methodology, Investigation. **Anna Sgarlata:** Validation, Software, Resources, Methodology, Investigation. **Luca Camilli:** Validation, Software, Resources, Methodology, Investigation. **Stephen O'Sullivan:** Validation, Investigation, Formal analysis, Data curation. **Vilas Patil:** Investigation, Formal analysis, Data curation. **Davinder Singh:** Validation, Software, Investigation, Formal analysis, Data curation. **Brendan Sheehan:** Validation, Software, Investigation, Formal analysis, Data curation. **Paul K. Hurley:** Visualization, Validation, Supervision, Resources, Project administration, Methodology, Funding acquisition, Conceptualization. **Lida Ansari:** Visualization, Validation, Supervision, Software, Resources, Methodology, Conceptualization. **Antonio Di Bartolomeo:** Writing – review & editing, Visualization, Validation, Supervision, Resources, Project administration, Funding acquisition. **Farzan Gity:** Writing – review & editing, Visualization, Validation, Supervision, Resources, Project administration, Methodology, Funding acquisition, Conceptualization.

Declaration of competing interest

The authors declare that they have no known competing financial interests or personal relationships that could have appeared to influence the work reported in this paper.

Acknowledgements

This work was supported by the Research Ireland (formerly Science Foundation Ireland) AMBER Research Centre (SFI-12/RC/2278_P2). This work was also partially supported by the Royal Academy of Engineering under the Research Fellowship Scheme grant number RF/201920/19/245. The SFI/HEA Irish Centre for High-End Computing (ICHEC) is acknowledged for the provision of computational facilities and support. H.N., S.J.K. and V.P. acknowledge funding through Irish Research Council (IRC) EPSPG/2023/1772, EU-MSCA project 101109772, and EU-MSCA project 101153933, respectively.

Appendix A. Supplementary data

Supplementary data to this article can be found online at https://doi.org/10.1016/j.mtadv.2025.100654.

Data availability

The data that support the findings of this study are available from the corresponding authors upon reasonable request.

References

[1] A. Di Bartolomeo, A. Kumar, O. Durante, A. Sessa, E. Faella, L. Viscardi, K. Intonti, F. Giubileo, N. Martucciello, P. Romano, S. Sleziona, M. Schleberger, Temperature-dependent photoconductivity in two-dimensional MoS2 transistors, Materials Today Nano (2023) 100382, https://doi.org/10.1016/j.mtnano.2023.100382.
[2] A. Pelella, K. Intonti, O. Durante, A. Kumar, L. Viscardi, S. De Stefano, P. Romano, F. Giubileo, H. Neill, V. Patil, L. Ansari, B. Roycroft, P.K. Hurley, F. Gity, A. Di Bartolomeo, Multilayer WS2 for low-Power visible and near-Infrared phototransistors, Discover Nano 19 (1) (2024) 57, https://doi.org/10.1186/s11671-024-04000-0.
[3] A. Kumar, L. Viscardi, E. Faella, F. Giubileo, K. Intonti, A. Pelella, S. Sleziona, O. Kharsah, M. Schleberger, A. Di Bartolomeo, Black phosphorus unipolar transistor, memory, and photodetector, J. Mater. Sci. 58 (6) (2023) 2689–2699, https://doi.org/10.1007/s10853-023-08169-0.
[4] Y.Y. Illarionov, T. Knobloch, M. Jech, M. Lanza, D. Akinwande, M.I. Vexler, T. Mueller, M.C. Lemme, G. Fiori, F. Schwierz, T. Grasser, Insulators for 2D nanoelectronics: the gap to bridge, Nat. Commun. 11 (1) (2020) 3385, https://doi.org/10.1038/s41467-020-16640-8.
[5] J. Yang, X. Liu, Q. Dong, Y. Shen, Y. Pan, Z. Wang, K. Tang, X. Dai, R. Wu, Y. Jin, W. Zhou, S. Liu, J. Sun, Oxidations of two-dimensional semiconductors: fundamentals and applications, Chin. Chem. Lett. 33 (1) (2022) 177–185, https://doi.org/10.1016/j.cclet.2021.06.078.
[6] G. Mirabelli, C. McGeough, M. Schmidt, E.K. McCarthy, S. Monaghan, I.M. Povey, M. McCarthy, F. Gity, R. Nagle, G. Hughes, A. Cafolla, P.K. Hurley, R. Duffy, Air

sensitivity of MoS2, MoSe2, MoTe2, HfS2, and HfSe2, J. Appl. Phys. 120 (12) (2016) 125102, https://doi.org/10.1063/1.4963290.
[7] M.J. Mleczko, C. Zhang, H.R. Lee, H.-H. Kuo, B. Magyari-Köpe, R.G. Moore, Z.-X. Shen, I.R. Fisher, Y. Nishi, E. Pop, HfSe 2 and ZrSe 2 : two-Dimensional Semiconductors with native High-κ oxides, Sci. Adv. 3 (2017) e1700481, https://doi.org/10.1126/sciadv.1700481.
[8] A. Molle, C. Grazianetti, L. Tao, D. Taneja, Md H. Alam, D. Silicene Akinwande, Silicene derivatives, and their device applications, Chem. Soc. Rev. 47 (16) (2018) 6370–6387, https://doi.org/10.1039/C8CS00338F.
[9] Y. Huang, J. Qiao, K. He, S. Bliznakov, E. Sutter, X. Chen, D. Luo, F. Meng, D. Su, J. Decker, W. Ji, R.S. Ruoff, P. Sutter, Interaction of black phosphorus with oxygen and water, Chem. Mater. 28 (22) (2016) 8330–8339, https://doi.org/10.1021/acs.chemmater.6b03592.
[10] F. Hou, D. Zhang, P. Sharma, S. Singh, T. Wu, J. Seidel, Oxidation kinetics of WTe2 surfaces in different environments, ACS Appl. Electron. Mater. 2 (7) (2020) 2196–2202, https://doi.org/10.1021/acsaelm.0c00380.
[11] Q. Li, Q. Zhou, L. Shi, Q. Chen, J. Wang, Recent advances in oxidation and degradation mechanisms of ultrathin 2D materials under ambient conditions and their passivation strategies, J. Mater. Chem. A 7 (9) (2019) 4291–4312, https://doi.org/10.1039/C8TA10306B.
[12] G. Wang, R. Pandey, S.P. Karna, Physics and chemistry of oxidation of two-dimensional nanomaterials by molecular oxygen, WIREs Comput. Mol. Sci. 7 (1) (2017) e1280, https://doi.org/10.1002/wcms.1280.
[13] P. Li, D. Zhang, J. Liu, H. Chang, Y. Sun, N. Yin, Air-stable black phosphorus devices for ion sensing, ACS Appl. Mater. Interfaces 7 (44) (2015) 24396–24402, https://doi.org/10.1021/acsami.5b07712.
[14] E. Long, S. O'Brien, E.A. Lewis, E. Prestat, C. Downing, C.S. Cucinotta, S. Sanvito, S.J. Haigh, V. Nicolosi, An in situ and Ex situ TEM study into the oxidation of titanium (IV) sulphide, npj 2D Mater Appl 1 (1) (2017) 1–9, https://doi.org/10.1038/s41699-017-0024-4.
[15] J. Hwang, J. Mun, K.-T. Lee, T. Lee, J. Kim, J. Min, K. Park, Impact of humidity on long-term stability of HfS2 grown on sapphire substrate by chemical vapor deposition and strategies to prevent native oxidation, Mater. Sci. Semicond. Process. 192 (2025) 109471, https://doi.org/10.1016/j.mssp.2025.109471.
[16] S.H. Chae, Y. Jin, T.S. Kim, D.S. Chung, H. Na, H. Nam, H. Kim, D.J. Perello, H. Y. Jeong, T.H. Ly, Y.H. Lee, Oxidation effect in octahedral hafnium disulfide thin film, ACS Nano 10 (1) (2016) 1309–1316, https://doi.org/10.1021/acsnano.5b06680.
[17] M. Zhang, Y. Zhu, X. Wang, Q. Feng, S. Qiao, W. Wen, Y. Chen, M. Cui, J. Zhang, C. Cai, L. Xie, Controlled synthesis of ZrS2 monolayer and few layers on hexagonal boron nitride, J. Am. Chem. Soc. 137 (22) (2015) 7051–7054, https://doi.org/10.1021/jacs.5b03807.
[18] S. Mañas-Valero, V. García-López, A. Cantarero, M. Galbiati, Raman spectra of ZrS2 and ZrSe2 from bulk to atomically thin layers, Appl. Sci. 6 (9) (2016) 264, https://doi.org/10.3390/app6090264.
[19] L. Chang, D.J. Frank, R.K. Montoye, S.J. Koester, B.L. Ji, P.W. Coteus, R. H. Dennard, W. Haensch, Practical strategies for power-efficient computing technologies, Proc. IEEE (2010), https://doi.org/10.1109/JPROC.2009.2035451.
[20] S.J. Kheirabadi, F. Behzadi, F. Gity, P.K. Hurley, S.K. Khorrami, M. Behroozi, M. Sanaee, L. Ansari, Defective ZrSe2: a promising candidate for spintronics applications, J. Phys. Condens. Matter 36 (13) (2023) 135501, https://doi.org/10.1088/1361-648X/ad13d3.
[21] A.C. Foucher, W. Mortelmans, W. Bing, Z. Sofer, R. Jaramillo, F.M. Ross, Structural changes in HfSe2 and ZrSe2 thin films with various oxidation methods, J. Mater. Chem. C 12 (26) (2024) 9677–9684, https://doi.org/10.1039/D3TC04698B.
[22] C. Xiong, Z. Yang, J. Shen, F. Tang, Q. He, Y. Li, M. Xu, X. Miao, Nano T-Se peninsulas embedded in natively oxidized 2D TiSe2 enable uniform and fast memristive switching, ACS Appl. Mater. Interfaces 15 (19) (2023) 23371–23379, https://doi.org/10.1021/acsami.3c00818.
[23] B.S.Y. Kim, T.D. Ngo, Y. Hassan, S.H. Chae, S.-G. Yoon, M.S. Choi, Advances and Applications of Oxidized van Der Waals Transition Metal Dichalcogenides, Adv. Sci. 11 (43) (2024) 2407175, https://doi.org/10.1002/advs.202407175.
[24] Xps OASIS. https://xpsoasis.org/. (Accessed 30 May 2025).
[25] S. Smidstrup, T. Markussen, P. Vancraeyveld, J. Wellendorff, J. Schneider, T. Gunst, B. Verstichel, D. Stradi, P.A. Khomyakov, U.G. Vej-Hansen, M.-E. Lee, S. T. Chill, F. Rasmussen, G. Penazzi, F. Corsetti, A. Ojanperä, K. Jensen, M.L. N. Palsgaard, U. Martinez, A. Blom, M. Brandbyge, K. Stokbro, QuantumATK: an integrated platform of electronic and atomic-scale modelling tools, J. Phys. Condens. Matter 32 (1) (2019) 015901, https://doi.org/10.1088/1361-648X/ab4007.
[26] M.J. van Setten, M. Giantomassi, E. Bousquet, M.J. Verstraete, D.R. Hamann, X. Gonze, G.-M. Rignanese, The PseudoDojo: training and grading a 85 element optimized norm-conserving pseudopotential table, Comput. Phys. Commun. 226 (2018) 39–54, https://doi.org/10.1016/j.cpc.2018.01.012.
[27] X.H. Zheng, J.X. Zheng, On the use of monkhorst–pack scheme to evaluate superconductivity and the issue of umklapp electron–phonon interactions, Phys. Chem. Chem. Phys. 25 (18) (2023) 13049–13060, https://doi.org/10.1039/D3CP01053H.
[28] S. Grimme, J. Antony, S. Ehrlich, H. Krieg, A consistent and accurate Ab initio parametrization of density functional dispersion correction (DFT-D) for the 94 elements H-Pu, J. Chem. Phys. 132 (15) (2010) 154104, https://doi.org/10.1063/1.3382344.
[29] J.H. Park, S. Vishwanath, X. Liu, H. Zhou, S.M. Eichfeld, S.K. Fullerton-Shirey, J. A. Robinson, R.M. Feenstra, J. Furdyna, D. Jena, H.G. Xing, A.C. Kummel, Scanning tunneling microscopy and spectroscopy of air exposure effects on molecular beam epitaxy grown WSe2 monolayers and bilayers, ACS Nano 10 (4) (2016) 4258–4267, https://doi.org/10.1021/acsnano.5b07698.
[30] P. Budania, P. Baine, J. Montgomery, C. McGeough, T. Cafolla, M. Modreanu, D. McNeill, N. Mitchell, G. Hughes, P. Hurley, Long-term stability of mechanically exfoliated MoS2 flakes, MRS Commun. 7 (4) (2017) 813–818, https://doi.org/10.1557/mrc.2017.105.
[31] H. Liu, N. Han, J. Zhao, Atomistic insight into the oxidation of monolayer transition metal dichalcogenides: from structures to electronic properties, RSC Adv. 5 (23) (2015) 17572–17581, https://doi.org/10.1039/c4ra17320a.
[32] S. Kc, R.C. Longo, R.M. Wallace, K. Cho, Surface oxidation energetics and kinetics on MoS2 monolayer, J. Appl. Phys. 117 (13) (2015) 135301, https://doi.org/10.1063/1.4916536.
[33] M.-Q. Ren, S. Han, J.-Q. Fan, L. Wang, P. Wang, W. Ren, K. Peng, S. Li, S.-Z. Wang, F.-W. Zheng, P. Zhang, F. Li, X. Ma, Q.-K. Xue, C.-L. Song, Semiconductor–metal phase transition and emergent charge density waves in 1T-ZrX2 (X = Se, Te) at the two-dimensional limit, Nano Lett. 22 (1) (2022) 476–484, https://doi.org/10.1021/acs.nanolett.1c04372.
[34] A.H. Reshak, S. Auluck, Theoretical investigation of the electronic and optical properties of ZrX2 (X=S, Se and Te), Phys. B Condens. Matter 353 (3) (2004) 230–237, https://doi.org/10.1016/j.physb.2004.10.001.
[35] A. Cruz, Z. Mutlu, M. Ozkan, C.S. Ozkan, Raman investigation of the air stability of 2H polytype HfSe2 thin films, MRS Commun. 8 (3) (2018) 1191–1196, https://doi.org/10.1557/mrc.2018.185.
[36] A. Di Bartolomeo, F. Urban, A. Pelella, A. Grillo, M. Passacantando, X. Liu, F. Giubileo, Electron irradiation of multilayer PdSe2 field effect transistors, Nanotechnology 31 (37) (2020) 375204, https://doi.org/10.1088/1361-6528/ab9472.
[37] W. Lu, Z. Li, M. Feng, H.-J. Yan, B. Yan, L. Hu, X. Zhang, S. Liu, J.-S. Hu, D.-J. Xue, Melt- and air-processed selenium thin-film solar cells, Sci. China Chem. 65 (11) (2022) 2197–2204, https://doi.org/10.1007/s11426-022-1332-3.
[38] L.I. Berger, Semiconductor Materials, CRC Press, London, 2020, https://doi.org/10.1201/9780138739966.
[39] Y. Xia, P. Yang, Y. Sun, Y. Wu, B. Mayers, B. Gates, Y. Yin, F. Kim, H. Yan, One-dimensional nanostructures: synthesis, characterization, and applications, Adv. Mater. 15 (5) (2003) 353–389, https://doi.org/10.1002/adma.200390087.
[40] B. Gates, B. Mayers, B. Cattle, Y. Xia, Synthesis and characterization of uniform nanowires of trigonal selenium, Adv. Funct. Mater. 12 (3) (2002) 219–227, https://doi.org/10.1002/1616-3028(200203)12:3%253C219::AID-ADFM219%253E3.0.CO;2-U.
[41] L. Liu, Q. Peng, Y. Li, Preparation of monodisperse Se colloid spheres and Se nanowires using Na2SeSO3 as precursor, Nano Res. 1 (5) (2008) 403–411, https://doi.org/10.1007/s12274-008-8040-5.
[42] H. Chen, D.-W. Shin, J.-G. Nam, K.-W. Kwon, J.-B. Yoo, Selenium nanowires and nanotubes synthesized via a facile template-free solution method, Mater. Res. Bull. 45 (6) (2010) 699–704, https://doi.org/10.1016/j.materresbull.2010.02.016.
[43] A. Rahman, G. Guisbiers, Synthesis of trigonal selenium rods, wires and fibers by pulsed laser ablation in ethanol, Mater. Lett. 377 (2024) 137476, https://doi.org/10.1016/j.matlet.2024.137476.
[44] Y. Yang, G. Niu, J. Lu, X. Geng, R. He, Y. Zhang, S. Li, Y. Zhang, L. Sun, L. Gao, J. Cai, From 2D AgTe monolayer to 1D AgTe nanowires: tellurium concentration modulated structural and electronic properties transformation, Small Methods (2024) e2402025, https://doi.org/10.1002/smtd.202402025.
[45] G. Niu, J. Lu, L. Gao, J. Geng, W. Xiong, Y. Zhang, H. Zhang, S. Li, Y. Yang, B. Fu, Y. Zhang, J. Cai, Atomically precise fabrication of ultranarrow zigzag CuTe nanoribbons via dimensional regulation, ACS Nano 19 (3) (2025) 3656–3664, https://doi.org/10.1021/acsnano.4c14204.
[46] L. Sun, C. Chen, Q. Zhang, C. Sohrt, T. Zhao, G. Xu, J. Wang, D. Wang, K. Rossnagel, L. Gu, C. Tao, L. Jiao, Suppression of the charge density wave state in two-dimensional 1T-TiSe2 by atmospheric oxidation, Angew. Chem. Int. Ed. 56 (31) (2017) 8981–8985, https://doi.org/10.1002/anie.201612605.
[47] B. Ghosh, M. Sahu, D. Samanta, G.D. Mukherjee, Strain-induced structural and electronic phase transitions in ZrSe2: high pressure X-Ray diffraction and raman studies, Bull. Mater. Sci. 45 (4) (2022) 221, https://doi.org/10.1007/s12034-022-02821-2.
[48] S.M. Oliver, J.J. Fox, A. Hashemi, A. Singh, R.L. Cavalero, S. Yee, D.W. Snyder, R. Jaramillo, H.-P. Komsa, P.M. Vora, Phonons and excitons in ZrSe2–ZrS2 alloys, J. Mater. Chem. C 8 (17) (2020) 5732–5743, https://doi.org/10.1039/D0TC00731E.
[49] A. Alsulami, M. Alharbi, F. Alsaffar, O. Alolaiyan, G. Aljalham, S. Albawardi, S. Alsaggaf, F. Alamri, T.A. Tabbakh, M.R. Amer, Lattice transformation from 2D to quasi 1D and phonon properties of exfoliated ZrS2 and ZrSe2, Small 19 (11) (2023) e2205763, https://doi.org/10.1002/smll.202205763.
[50] A.H. Goldan, C. Li, S.J. Pennycook, J. Schneider, A. Blom, W. Zhao, Molecular structure of vapor-deposited amorphous selenium, J. Appl. Phys. 120 (13) (2016) 135101, https://doi.org/10.1063/1.4962315.
[51] W. Lu, Z. Li, M. Feng, L. Zheng, S. Liu, B. Yan, J.-S. Hu, D.-J. Xue, Structure of amorphous selenium: small ring, big controversy, J. Am. Chem. Soc. 146 (9) (2024) 6345–6351, https://doi.org/10.1021/jacs.4c00219.
[52] P. Tsipas, D. Tsoutsou, J. Marquez-Velasco, K.E. Aretouli, E. Xenogiannopoulou, E. Vassalou, G. Kordas, A. Dimoulas, Epitaxial ZrSe2/MoSe2 semiconductor v.d. waals heterostructures on wide band gap AlN substrates, Microelectron. Eng. 147 (2015) 269–272, https://doi.org/10.1016/j.mee.2015.04.113.
[53] D. Barreca, G.A. Battiston, R. Gerbasi, E. Tondello, P. Zanella, Zirconium dioxide thin films characterized by XPS, Surf. Sci. Spectra 7 (4) (2000) 303–309, https://doi.org/10.1116/1.1375573.

[54] D. Chavez, A.D. Berube, L.M. Davis, Zirconium disulfide single crystal, ZrS2(0001), characterized by X-Ray photoelectron spectroscopy, Surf. Sci. Spectra 32 (1) (2025) 014004, https://doi.org/10.1116/6.0004276.
[55] R. Yue, A.T. Barton, H. Zhu, A. Azcatl, L.F. Pena, J. Wang, X. Peng, N. Lu, L. Cheng, R. Addou, S. McDonnell, L. Colombo, J.W.P. Hsu, J. Kim, M.J. Kim, R.M. Wallace, C.L. Hinkle, HfSe2 thin films: 2D transition metal dichalcogenides grown by molecular beam epitaxy, ACS Nano 9 (1) (2015) 474–480, https://doi.org/10.1021/nn5056496.
[56] Y.Y. Wang, Z.H. Ni, Z.X. Shen, H.M. Wang, Y.H. Wu, Interference enhancement of raman signal of graphene, Appl. Phys. Lett. 92 (4) (2008) 043121, https://doi.org/10.1063/1.2838745.
[57] C. Lee, H. Yan, L.E. Brus, T.F. Heinz, J. Hone, S. Ryu, Anomalous lattice vibrations of Single- and few-layer MoS2, ACS Nano 4 (5) (2010) 2695–2700, https://doi.org/10.1021/nn1003937.
[58] L. Cui, R. He, G. Li, Y. Zhang, Y. You, M. Huang, Raman spectroscopy of optical phonon and charge density wave modes in 1T-TiSe2 exfoliated flakes, Solid State Commun. 266 (2017) 21–25, https://doi.org/10.1016/j.ssc.2017.08.014.
[59] S.-L. Li, H. Miyazaki, H. Song, H. Kuramochi, S. Nakaharai, K. Tsukagoshi, Quantitative raman spectrum and reliable thickness identification for atomic layers on insulating substrates, ACS Nano 6 (8) (2012) 7381–7388, https://doi.org/10.1021/nn3025173.
[60] A. Di Bartolomeo, A. Grillo, F. Urban, L. Iemmo, F. Giubileo, G. Luongo, G. Amato, L. Croin, L. Sun, S.-J. Liang, L.K. Ang, Asymmetric schottky contacts in bilayer MoS_2 field effect transistors, Adv. Funct. Mater. 28 (28) (2018) 1800657, https://doi.org/10.1002/adfm.201800657.
[61] A. Grillo, A. Di Bartolomeo, A current–voltage model for double schottky barrier devices, Adv. Electron. Mater. 7 (2) (2021) 2000979, https://doi.org/10.1002/aelm.202000979.
[62] Intonti, K.; Faella, E.; Viscardi, L.; Kumar, A.; Durante, O.; Giubileo, F.; Passacantando, M.; Lam, H. T.; Anastasiou, K.; Craciun, M. F.; Russo, S.; Di Bartolomeo, A. Hysteresis and photoconductivity of few-layer ReSe2 field effect transistors enhanced by air pressure. Adv. Electron. Mater. n/a (n/a), 2300066. https://doi.org/10.1002/aelm.202300066.
[63] K. Intonti, E. Coleman, A. Blake, C. Lyons, A. Hydes, A. Di Bartolomeo, F. Gity, P. Hurley, Role of interface and bulk traps on the capacitance-voltage characteristics of Ws2/Al2o3/Si capacitors, Rochester, NY (April 25, 2023), https://doi.org/10.2139/ssrn.4429239.
[64] J.W. John, A. Mishra, R. Debbarma, I. Verzhbitskiy, K.E.J. Goh, Probing charge traps at the 2D semiconductor/dielectric interface, Nanoscale 15 (42) (2023) 16818–16835, https://doi.org/10.1039/D3NR03453D.
[65] F. Volmer, I. Seidler, T. Bisswanger, J.-S. Tu, L.R. Schreiber, C. Stampfer, B. Beschoten, How to solve problems in Micro- and nanofabrication caused by the emission of electrons and charged metal atoms during e-Beam evaporation, J. Phys. D Appl. Phys. 54 (22) (2021) 225304, https://doi.org/10.1088/1361-6463/abe89b.
[66] C. Lee, S. Rathi, M.A. Khan, D. Lim, Y. Kim, S.J. Yun, D.-H. Youn, K. Watanabe, T. Taniguchi, G.-H. Kim, Comparison of trapped charges and hysteresis behavior in hBN encapsulated single MoS2 flake based field effect transistors on SiO2 and hBN substrates, Nanotechnology 29 (33) (2018) 335202, https://doi.org/10.1088/1361-6528/aac6b0.
[67] A. Mazzotti, K. Intonti, L. Viscardi, O. Durante, A. Spuri, A. Di Bernardo, A. Di Bartolomeo, Two-dimensional MoS2 logic inverter, in: 2025 IEEE 25th International Conference on Nanotechnology (NANO), 2025, pp. 255–260, https://doi.org/10.1109/NANO63165.2025.11113683.
[68] A. Sebastian, R. Pendurthi, T.H. Choudhury, J.M. Redwing, S. Das, Benchmarking monolayer MoS2 and WS2 field-effect transistors, Nat. Commun. 12 (1) (2021) 693, https://doi.org/10.1038/s41467-020-20732-w.
[69] L. Viscardi, K. Intonti, A. Kumar, E. Faella, A. Pelella, F. Giubileo, S. Sleziona, O. Kharsah, M. Schleberger, A. Di Bartolomeo, Black phosphorus nanosheets in field effect transistors with Ni and NiCr contacts, Phys. Status Solidi 260 (9) (2023) 2200537, https://doi.org/10.1002/pssb.202200537.
[70] K. Reidy, W. Mortelmans, S.S. Jo, A.N. Penn, A.C. Foucher, Z. Liu, T. Cai, B. Wang, F.M. Ross, R. Jaramillo, Atomic-scale mechanisms of MoS2 oxidation for kinetic control of MoS2/MoO3 interfaces, Nano Lett. 23 (13) (2023) 5894–5901, https://doi.org/10.1021/acs.nanolett.3c00303.